University of Nevada

Reno

A TWO-DIMENSIONAL SIMULATION OF TRITIUM TRANSPORT IN THE VADOSE ZONE AT THE NEVADA TEST SITE

A thesis submitted in partial fulfillment

of the requirements for the degree of

Master of Science in Hydrogeology

by

Wyn Charles Ross

The thesis of Wyn Charles Ross is approved:

Thesis advisor

Department Chairman

Dean, Graduate School

University of Nevada

Reno

April 1990

ACKNOWLEDGEMENTS

I would like to express my sincere appreciation to the members of my graduate committee: Dr. Stephen Wheatcraft, Dr. Roger Jacobsen, and Dr. Robert Watters for their assistance throughout the course of this research.

"Life is *sooooo* strange" (Duncan, P. 1985. Personal Communication)

I would also like to thank the gang on the back hall who helped make my stay in Reno so much fun. You know who you are.

ABSTRACT

The site of a 0.75 kiloton underground nuclear explosion, the Cambric event, was selected for the study of radionuclide transport in the hydrologic environment. Water samples from RNM-2S, a well located 91 m from Cambric, have been analyzed for tritium and other radionuclides since the initiation of pumping. Water from RNM-2S flows to Frenchman Lake via an unlined canal. Flume data indicate canal transmission losses of approximately 2 m^3/day/meter of canal.

To determine if infiltrating canal water might be recirculated by RNM-2S, and therefore provide an additional radionuclide input to water samples collected at RNM-2S, a two-dimensional variably saturated solute transport computer model [SATURN, Huyakorn et al., 1983] was used to simulate the movement of tritium from the canal to the water table.

Results indicate that recirculated canal water has not had a significant effect on the breakthrough of tritium at RNM-2S.

CONTENTS

LIST OF FIGURES

LIST OF TABLES

INTRODUCTION

General

The Radionuclide Migration (RNM) Project was initiated in 1974 by the Nevada Operations Office of the Department of Energy to study the distribution of radionuclides around an underground nuclear cavity. The goals of the RNM project were to determine the rates of migration of radionuclides in a variety of underground media at the Nevada Test Site (NTS) and to determine the potential for movement both on and off the NTS of radiation from underground nuclear explosions. The possible contamination of water supplies was of particular concern.

The site of a .75 kiloton underground nuclear test, the Cambric Event, was selected for the study. The Cambric test was conducted on May 14, 1965 in the tuffaceous alluvium of Frenchman Flat. The detonation point was 73 m below the water table, at a depth of 294 m.

The Cambric site was selected for the following reasons:

- The event took place within the NTS area 5 water supply aquifer
- Sufficient time had elapsed since the detonation for water in the cavity and rubble chimney to return to the preshot level
- The site is far from areas of active nuclear testing

- The detonation point is fairly close to the ground surface making re-entry drilling and sampling less difficult and expensive
- The highly permeable alluvium with its lack of fractures would make a good medium for hydrologic studies
- The chimney region contained uranium, plutonium, and fission products
- Sufficient tritium was present to constitute an excellent tracer for water from the cavity region

A re-entry well (RNM-1) was completed in May 1974 and samples were taken to determine the radionuclide content of the water and the postshot debris. A second well (RNM-2S) was positioned 91 m from the Cambric cavity (Figure 1). Pumping of RMN-2S was initiated in October 1975 to induce a hydraulic gradient from the Cambric cavity and provide an opportunity for study of radionuclide migration under field conditions. Water from RNM-2S is piped to an unlined canal which runs approximately 1.6 km to the north end of Frenchman Lake where the water discharges to a bermed area near the playa. Figure 2 is a map of West-central Frenchman Flat.

RNM-2S has been pumped almost continuously since 1975. Water samples from RNM-2S have been analyzed for tritium and other radionuclides at weekly or biweekly intervals since the initiation of pumping.

Three Parshall flumes were installed along the canal at the positions shown in Figure 3. Data from these flumes indicate that there is significant transmission loss along the canal (Figure 4). If the infiltrating canal water is captured by RNM-2S, it would constitute an additional source of tritium to the well, thereby affecting the

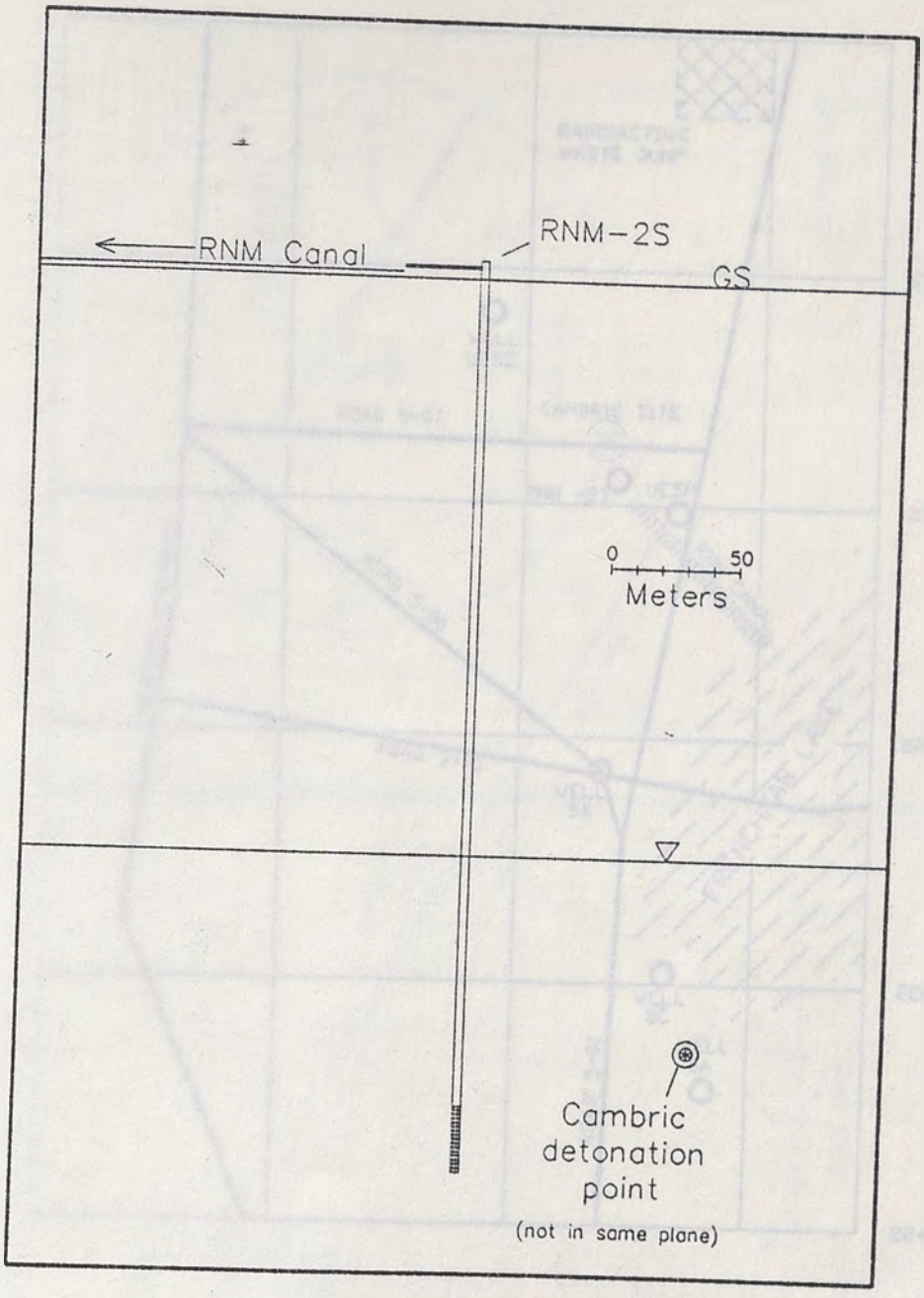

Figure 1. Cross section showing RNM-2S and the Cambric detonation point.

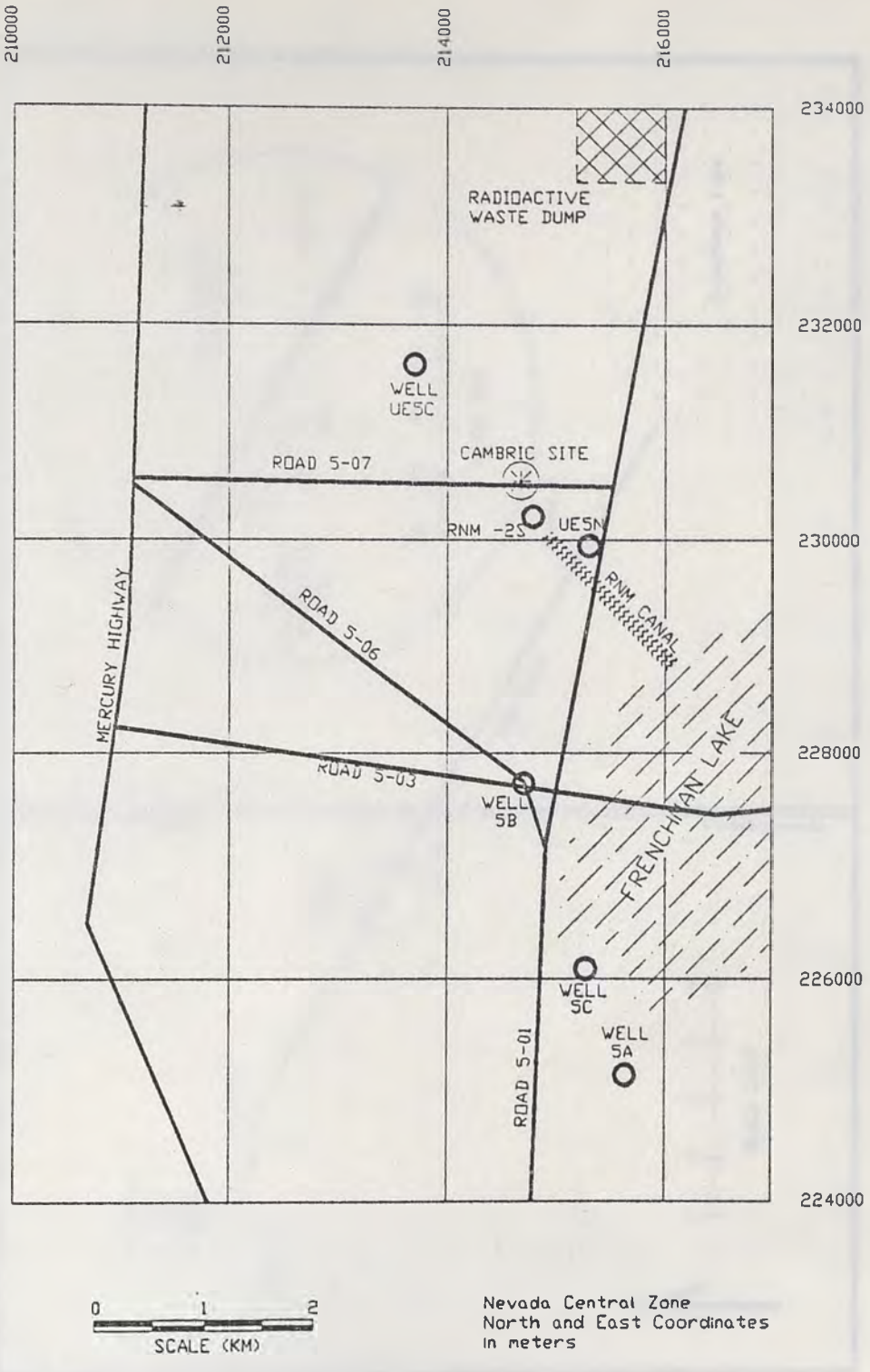

Figure 2. Map of West-central Frenchman Flat showing location of RNM site (after Hoffman et al., 1977)

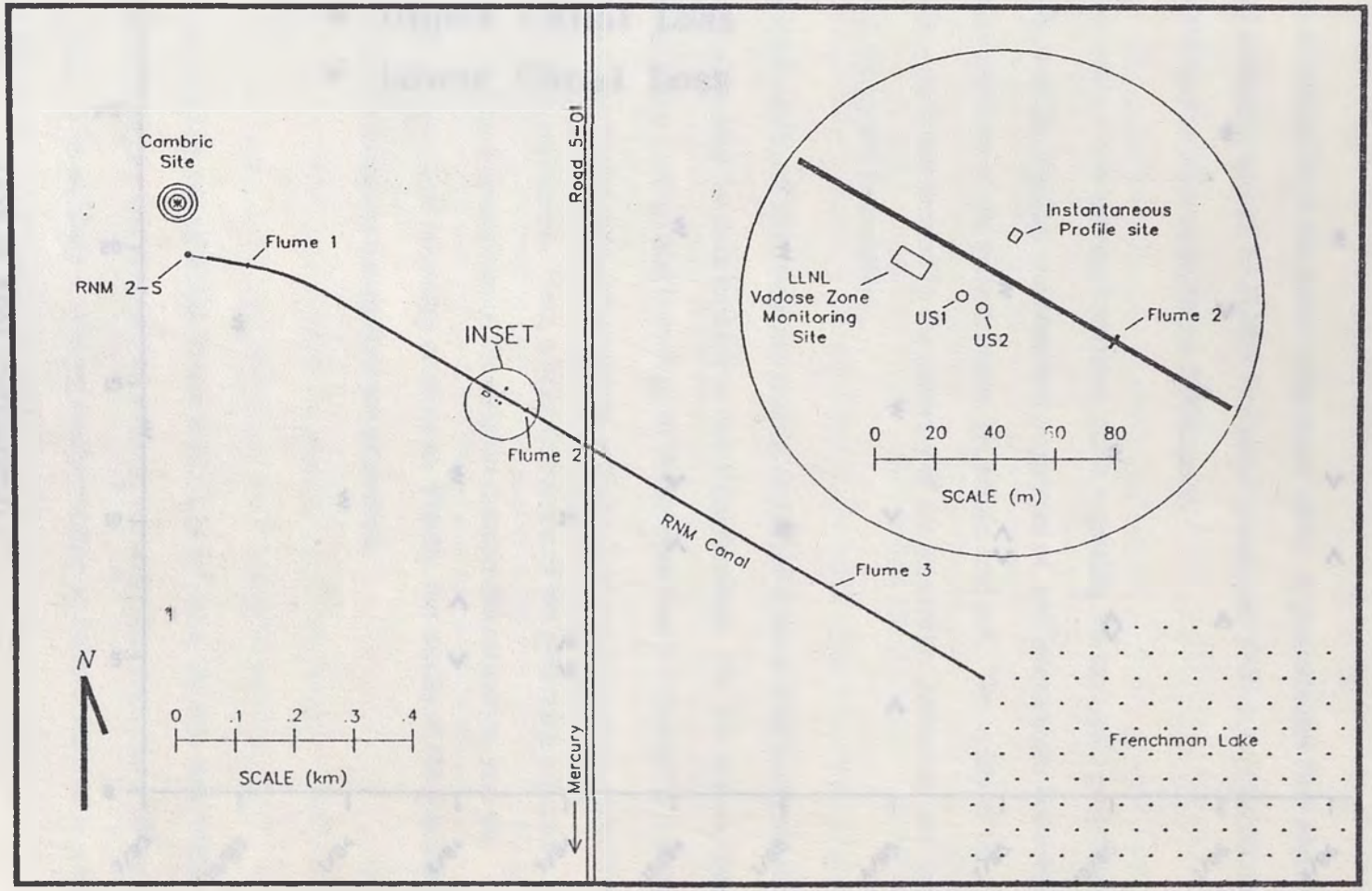

Figure 3. Cambric Site of the Radionuclide Migration Project

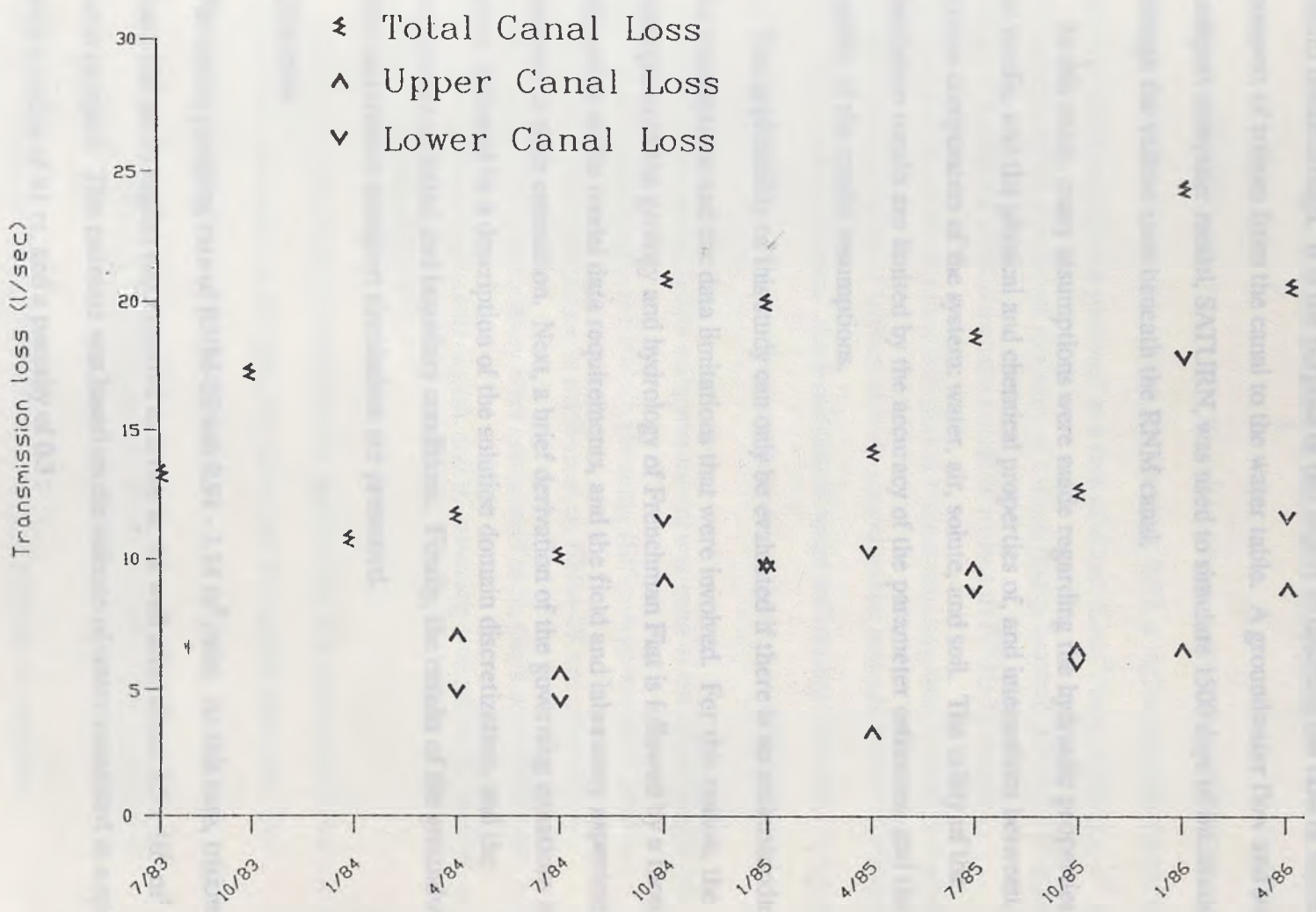

Figure 4. RNM Canal transmission losses.

tritium breakthrough. It is the purpose of this report to describe the flow of water and transport of tritium from the canal to the water table. A groundwater flow and solute transport computer model, SATURN, was used to simulate 1500 days of infiltration through the vadose zone beneath the RNM canal.

In this study, many assumptions were made regarding the hydraulic properties of the media, and the physical and chemical properties of, and interactions between, the various components of the system: water, air, solute, and soil. The utility of the simulation results are limited by the accuracy of the parameter estimates, and the validity of the model assumptions.

The applicability of this study can only be evaluated if there is an understanding of the assumptions and the data limitations that were involved. For this reason, the description of the geology and hydrology of Frenchman Flat is followed by a thorough discussion of the model data requirements, and the field and laboratory experiments involved in their estimation. Next, a brief derivation of the governing equations is given, followed by a description of the solution domain discretization, and the assignment of initial and boundary conditions. Finally, the results of the groundwater flow and tritium transport simulations are presented.

Objective

The initial pumping rate of RNM-2S was 0.94 - 1.14 m^3/min. At this rate, tritium from the cavity region was expected to arrive at the well after about 9.5 x 10^5 m^3 had been pumped. This estimate was based on the volume of water contained in a sphere with a radius of 91 m, and a porosity of 0.3 :

$$V = \frac{4}{3}\pi r^3 n = \frac{4}{3}\pi 91m^3 .3 = 9.5 \times 10^5 m^3 \quad (1)$$

By August 1977, more than 1.14×10^6 m^3 had been pumped from RNM-2S without detection of Cambric tritium. In October 1977, a higher capacity pump was installed and pumping was resumed at a rate of about 2.3 m^3/min. After 2×10^6 m^3 had been pumped, significant amounts of tritium finally reached RNM-2S (Figures 5 and 6). Theories to explain the late arrival of tritium at RNM-2S include: inhomogeneities in the aquifer; diffusion of tritium into stagnant, immobile regions in the flow path; exchange of tritium with structural water; and adsorption of tritium on the surface of clay particles. Recirculation of water infiltrating from the discharge canal might also have had an affect on tritium breakthrough at RNM-2S.

A three-dimensional solute transport model was used to simulate tritium and chloride-36 breakthrough at RNM-2S [Burbey, 1984]. A good match between simulated and observed tritium breakthrough at RNM-2S was achieved by incorporating a low permeability layer (presumed to be playa type sediments) between the pump intake and the cavity region, and by assuming a distribution coefficient for tritium of 0.8 ml/g (Figure 7).

Distribution coefficients represent the partitioning of a contaminant between the solution and the solids, in this case, the water and the aquifer material. The distribution coefficient can be represented as

$$K_d = \frac{\text{mass of solute on the solid phase per unit mass of solid phase}}{\text{concentration of solute in solution}} \quad (2)$$

A high distribution coefficient indicates a strong tendency for sorption.

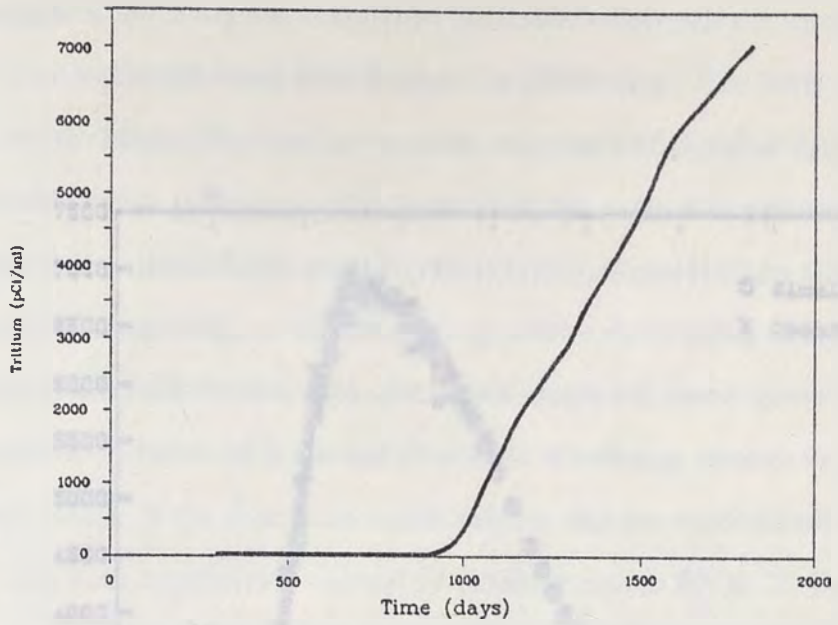

Figure 5. Tritium concentration (corrected to Cambric zero time) at RNM-2S vs time (after Daniels, 1981)

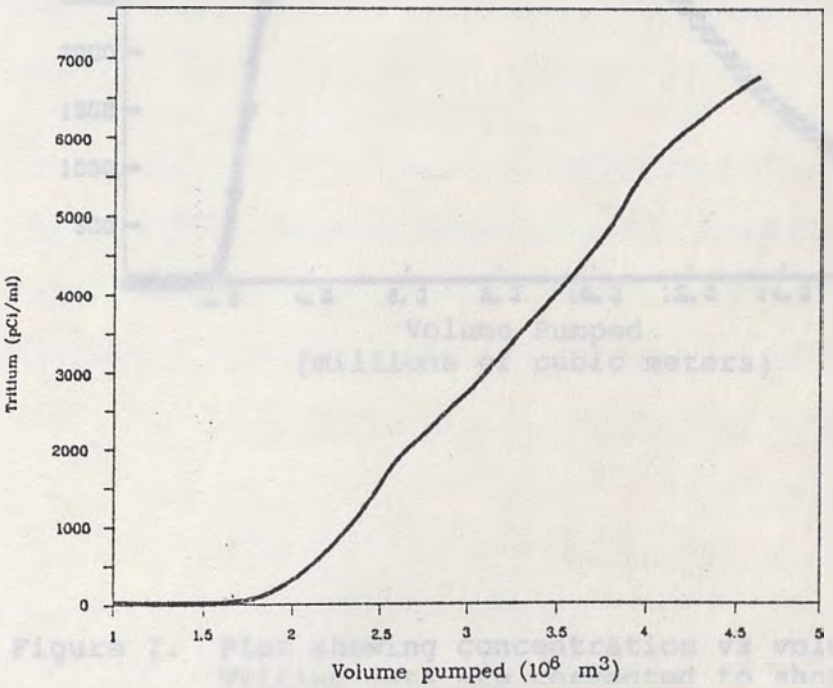

Figure 6. Tritium concentration (corrected to Cambric zero time) at RNM-2S vs volume pumped (after Daniels, 1981).

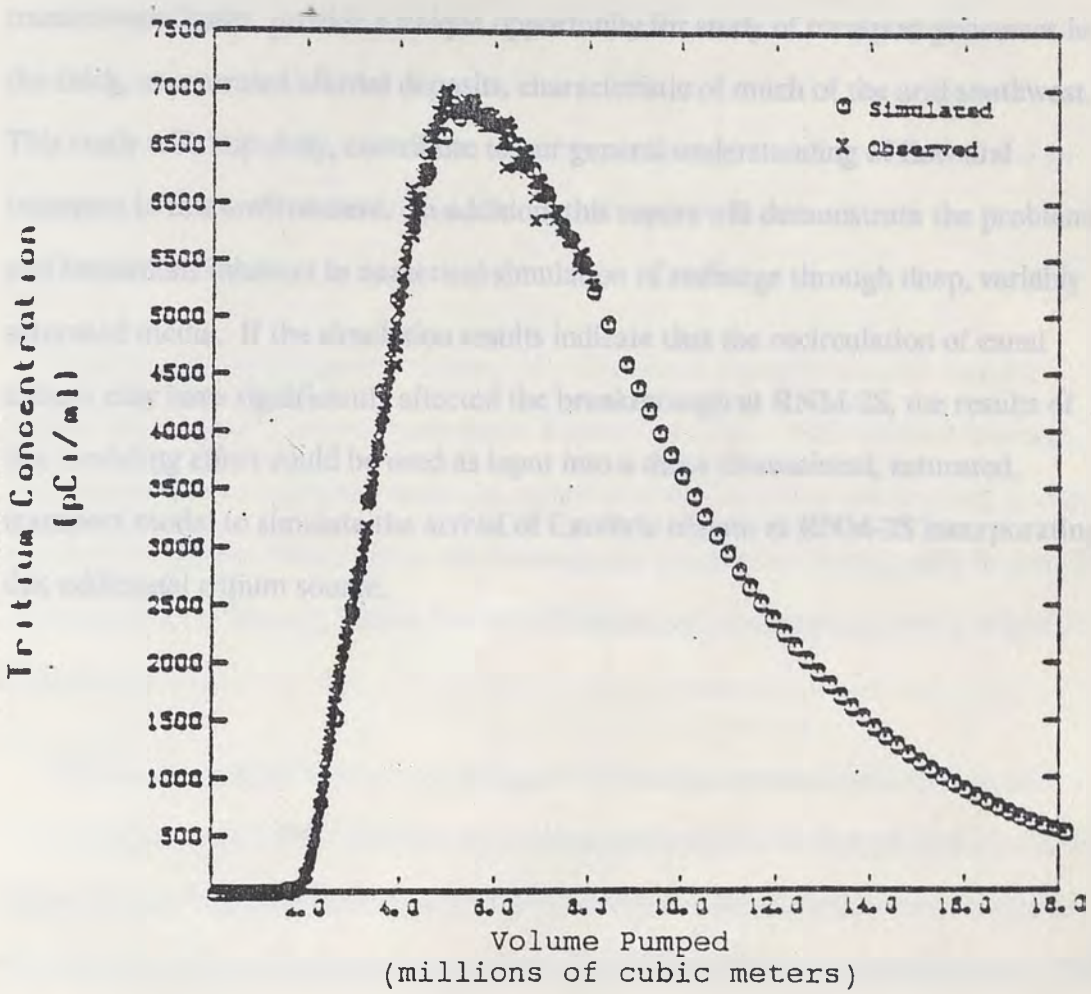

Figure 7. Plot showing concentration vs volume pumped. Tritium data are corrected to shot time. After Burbey, 1984.

The goal of this study was to describe the flow of water and the transport of Cambric tritium to the water table beneath the RNM canal. The fairly complete record of the radionuclide input to the canal, together with detailed data on the canal transmission losses, provide a unique opportunity for study of transport processes in the thick, unsaturated alluvial deposits, characteristic of much of the arid southwest. This study will, hopefully, contribute to our general understanding of flow and transport in this environment. In addition, this report will demonstrate the problems and limitations inherent in numerical simulation of recharge through deep, variably saturated media. If the simulation results indicate that the recirculation of canal tritium may have significantly affected the breakthrough at RNM-2S, the results of this modeling effort could be used as input into a three dimensional, saturated, transport model to simulate the arrival of Cambric tritium at RNM-2S incorporating this additional tritium source.

HYDROGEOLOGY

Location

The Nevada Test Site, an area of about 3600 km^2, is located approximately 110 km northwest of Las Vegas in the Nevada desert. This area is in the southernmost part of the Great Basin section of the Basin and Range physiographic province defined by Fenneman [1931]. Frenchman Flat, the site of the Cambric event, is in the southeast portion of the Test Site.

Frenchman Flat is a gently sloping (10 - 12 m/km) closed basin with interior surface drainage to a normally dry playa, Frenchman Lake. Well defined drainage channels in the mountainous areas and upper alluvial slopes become braided as they approach the lower desert floor. All channels are ephemeral, flowing only in response to precipitation. Runoff, rapidly lost to infiltration and evaporation, rarely reaches Frenchman Lake.

The study area lies in the most arid part of Nevada, the most arid state in the Union [Winograd, 1971]. The average annual precipitation on Frenchman Flat is only about 15 cm. The potential annual evaporation from lake and reservoir surfaces in this area has been estimated to range from 152 -208 cm [Meyers and Nodenson, 1962].

Geology

Frenchman Flat lies in the transitional zone between the Tertiary volcanic rocks of south-central Nevada and the Paleozoic rocks, primarily carbonates, that characterize eastern Nevada. Ranges to the south, southeast, and east of Frenchman Flat consist

of lower Paleozoic limestone, dolomite, and quartzite. Tertiary volcanics, mostly tuffs, compose the hills to the north and west.

Erosion and sedimentation have filled the valley with alluvium and playa sediments. In central Frenchman Flat, the alluvium is at least 500 m thick and probably reaches a maximum thickness of 700 to 800 m [Hoffman et al, 1977]. Figure 8 shows a cross section of the geology at the Cambric site along the section indicated in Figure 9 (the depths to Tertiary and Paleozoic rocks are speculative). For detailed information on the geology of the Nevada Test Site, the reader is referred to Winograd [1971], Carr [1975].

Hydrology

Frenchman Flat lies within the Ash Meadows groundwater system, an 11,500 km^2 area in which water flows in a southwesterly direction to discharge at Ash Meadows in the Amargosa Desert.

Winograd et al. [1971] grouped the numerous geologic formations and members of the Nevada Test Site region into units of hydrologic significance. The resulting 10 hydrogeologic units in order of decreasing age are: lower clastic aquitard; lower carbonate aquifer; upper clastic aquitard; upper carbonate aquifer; tuff aquitard; lava-flow aquitard; bedded tuff aquifer; welded tuff aquifer; lava-flow aquifer; and valley-fill aquifer. This study considers flow only in the valley-fill aquifer. For detailed description of the other hydrogeologic units, see Winograd [1977].

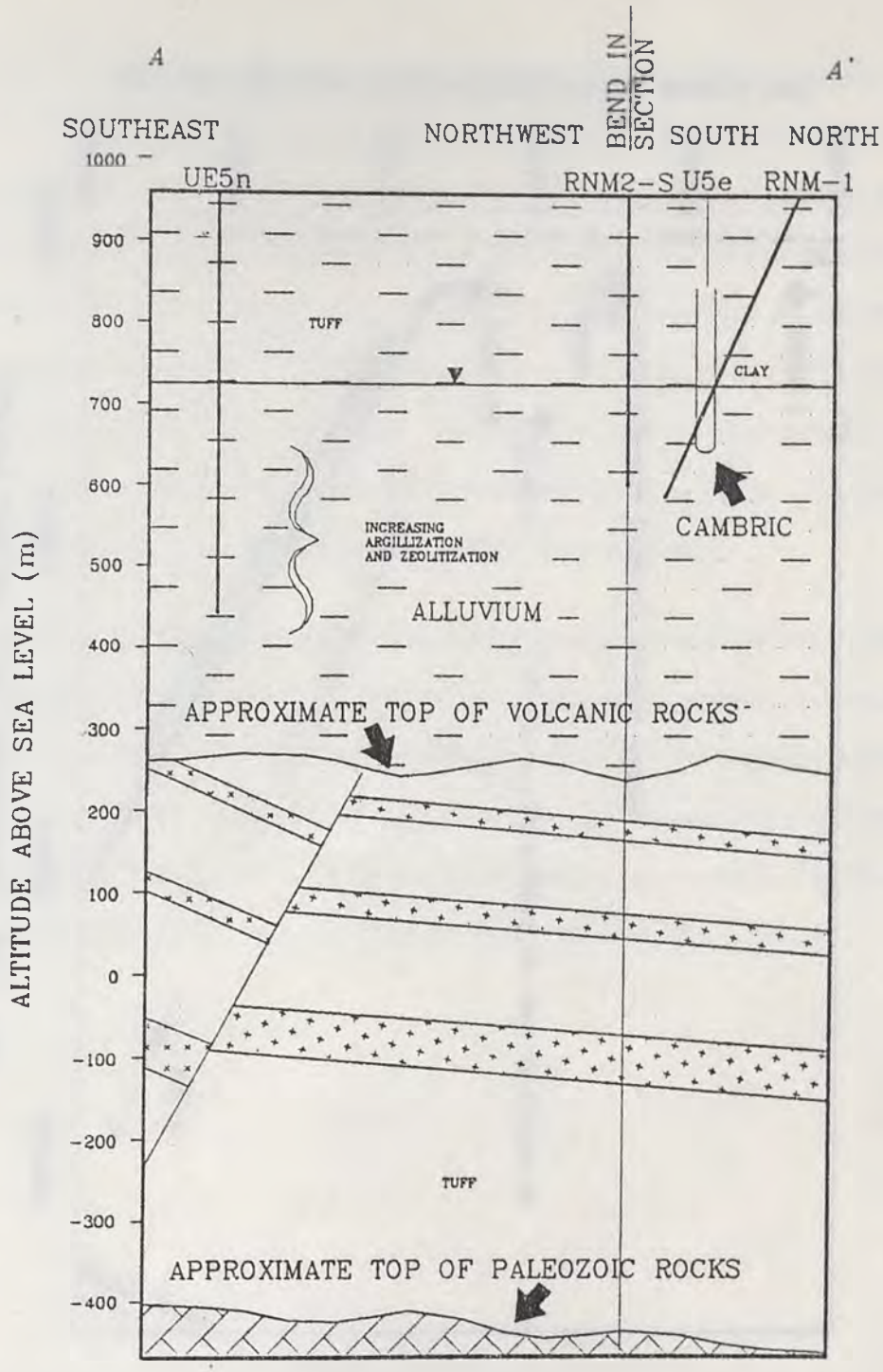

Figure 8. Geologic section at RNM site (after Hoffman et al., 1977) See Figure 10 for the location of section line A–A'.

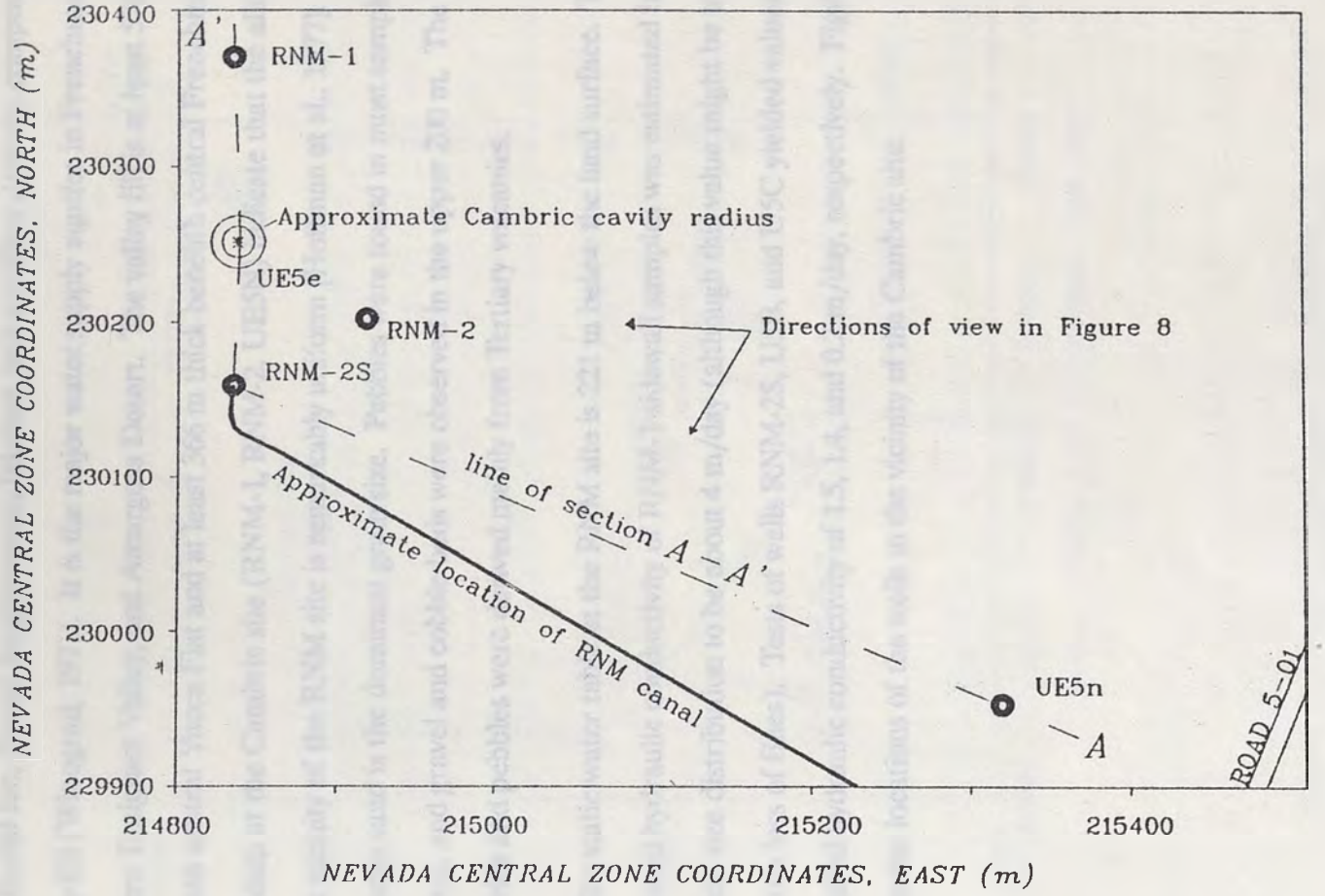

Figure 9. Location of section line $A-A'$ (Figure 8). After Hoffman et al, 1977.

Alluvial fan, fluvial, fanglomerate, lakebed, and mudflow deposits compose the valley-fill [Winograd, 1971]. It is the major water supply aquifer in Frenchman Flat, western Emigrant Valley, and Amargosa Desert. The valley fill is at least 570 m thick beneath central Yucca Flat and at least 366 m thick beneath central Frenchman Flat. Well data at the Cambric site (RNM-1, RNM-2, UE5N) indicate that the alluvial fill in the vicinity of the RNM site is remarkably uniform [Hoffman et al., 1977]. Medium to coarse sand is the dominant grain size. Pebbles were found in most samples and cuttings, and gravel and cobble beds were observed in the upper 200 m. The sand particles and pebbles were derived mainly from Tertiary volcanics.

The static water table at the RNM site is 221 m below the land surface. The saturated hydraulic conductivity of RNM-1 sidewall samples was estimated from particle size distribution to be about 4 m/day (although this value might be too high due to a loss of fines). Tests of wells RNM-2S, U5B, and U5C yielded values of saturated hydraulic conductivity of 1.5, 1.4, and 0.2 m/day, respectively. Figure 10 shows the locations of the wells in the vicinity of the Cambric site.

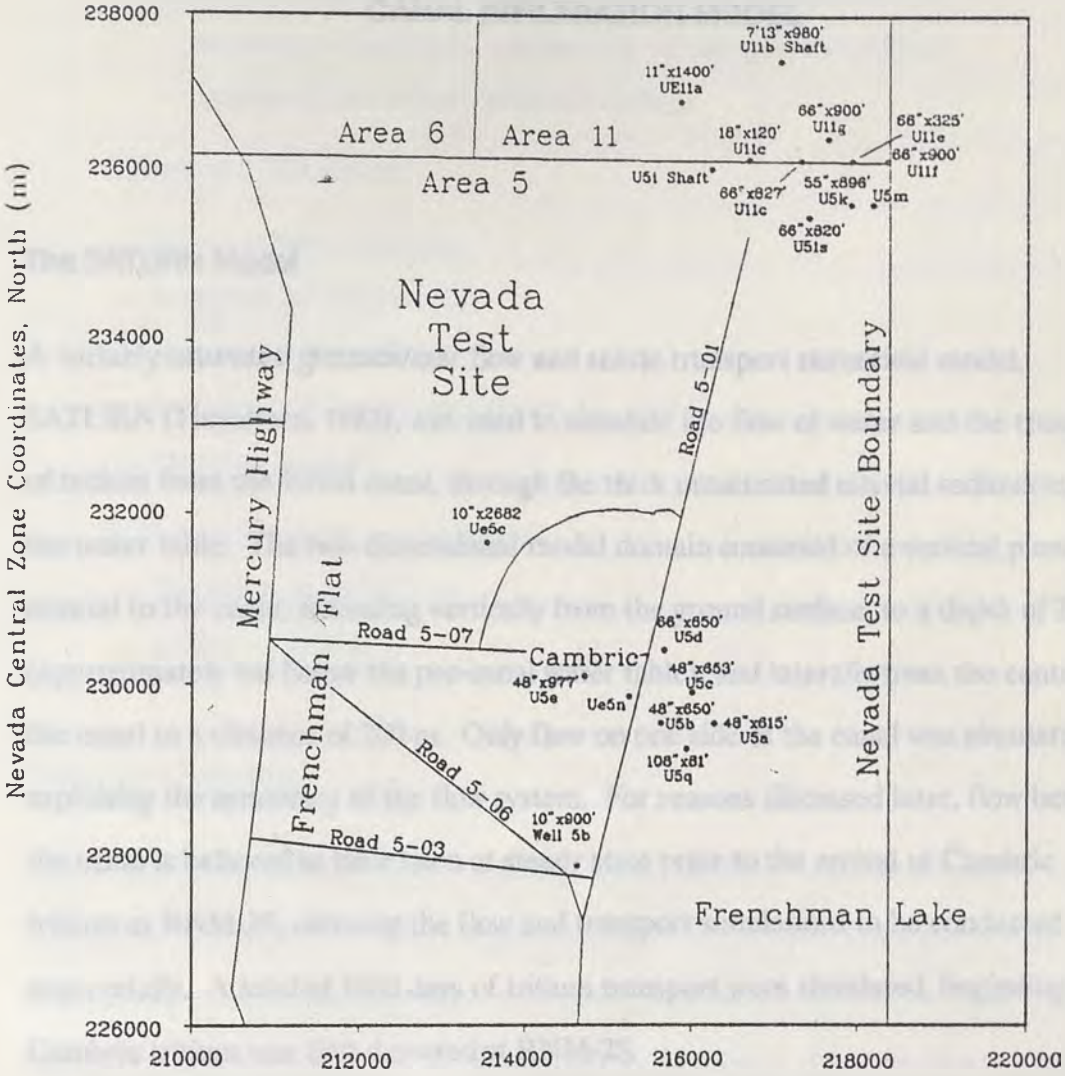

Figure 10 Map of Frenchman Flat showing the locations of drill holes (after Ramspott, 1977).

CANAL INFILTRATION MODEL

The SATURN Model

A variably saturated groundwater flow and solute transport numerical model, SATURN (Huyakorn, 1983), was used to simulate the flow of water and the transport of tritium from the RNM canal, through the thick unsaturated alluvial sediments, to the water table. The two-dimensional model domain consisted of a vertical plane, normal to the canal, extending vertically from the ground surface, to a depth of 225 m (approximately 4m below the pre-canal water table), and laterally from the center of the canal to a distance of 200 m. Only flow on one side of the canal was simulated, exploiting the symmetry of the flow system. For reasons discussed later, flow beneath the canal is believed to have been at steady state prior to the arrival of Cambric tritium at RNM-2S, allowing the flow and transport simulations to be conducted sequentially. A total of 1500 days of tritium transport were simulated, beginning when Cambric tritium was first detected at RNM-2S.

SATURN Input Requirements

Input data for SATURN include the following:

1. Flow Simulation--porous media properties.
   - Saturated hydraulic conductivity components , K_{xx}, K_{zz}, K_{xz}

- Saturated specific storage
- Effective porosity
- Tabulated data of, or parameters of analytical expressions for;
  - unsaturated hydraulic conductivity versus moisture content
  - matric suction versus moisture content

2.Transport Simulation.

A. Porous media properties

- Longitudinal dispersivity
- Transverse dispersivity
- Molecular diffusion coefficients, D_{xx} and D_{zz}
- Effective porosity

B. Properties of the solute species

- Retardation coefficient
- Initial inventory

Parameter Estimation

Input data for the porous media properties were based on field and laboratory tests, and on the literature. Input data regarding properties of water and tritium were from the literature. Saturated hydraulic conductivity was measured both in the field and in the laboratory, and compared to values from the literature. The unsaturated hydraulic conductivity function, and the soil moisture characteristic were measured in situ by the instantaneous profile method [Hillel, 1972]. Values of parameters in the analytical expressions relating matric suction and unsaturated hydraulic conductivity to moisture content were then determined by regression analysis [van Genuchten, 1978], and compared with the field measurements.

Laboratory Saturated Hydraulic Conductivity Determination Core samples from holes US1 and US2 (Figure 3) were used to determine the saturated hydraulic conductivity of the alluvium. At three meter intervals, one meter of 10 cm diameter core was taken, where possible. The core was collected in brass sample sleeves, in 7.6 cm and 15.2 cm sections. Each section was separated with a knife and sealed with plastic end caps in the field.

The grain size distribution of sidewall samples from RNM-1 was used to calculate an average hydraulic conductivity for the alluvium of about 4 m/day--although this estimate may be too high due to loss of fines. Tests of wells RNM-2S, U5B, and U5C yielded conductivities of 1.5 m/day, 1.4 m/day, and 0.2 m/day, respectfully [Hoffman et al., 1977]. Klute [1965] suggests a constant head permeameter be used for samples with conductivities greater than approximately 0.14 m/day, and falling head methods for samples with lower conductivities.

A constant head permeameter was constructed for the testing. A pair of end caps were equipped with inflow and outflow fittings, allowing the cores to be tested in the sample sleeves, thus minimizing the disturbance of the sample, and preserving as much of the soil structure as possible. Blocking of sample pores by air can result in sizable error in permeameter measurements. The entrapment of air in a sample during saturation will result in a falsely low measured conductivity. To avoid this, interstitial air in the cores was displaced with carbon dioxide prior to saturation. Carbon dioxide (CO_2) is far more soluble in water than air. For example, at 25° C., 759 ml. of CO_2 can be absorbed by one liter of water (this is the volume of gas when reduced to 0° C. and 760 mm Hg.). Under similar conditions, only about 17 ml. of air can be dissolved in the same volume of water. In addition, the samples were saturated

under a vacuum, from the bottom. According to Lambe [1957], this procedure reduces the amount of entrapped gas in the sample. To prevent any gas from coming out of solution during testing, degassed water was used. The results of the permeameter testing are given in Figure 11. After the permeameter testing, the saturated soil cores were weighed and oven dried at 105° C. to determine the porosity. Porosity and saturated hydraulic conductivity data are presented in Table 1.

Unsaturated Properties of the Porous Medium Quantitative description of unsaturated flow requires a knowledge of the water retention characteristics of the soil involved, and the functional dependence of hydraulic conductivity on moisture content or matric suction.

The difficulties associated with the direct measurement of unsaturated hydraulic conductivity have created substantial interest in methods of determining the hydraulic conductivity of an unsaturated soil from characteristics that are more easily quantified. According to Mualem [1976], these methods are of two types. The first relates the hydraulic conductivity to the soil characteristic [Childs and Collis-George, 1950; Marshall, 1958; Millington and Quirk, 1961; Jackson et al., 1965; Kunze et al., 1968; Farrell and Larson, 1972]. The second method assumes that the hydraulic conductivity is a power function of the effective saturation [Brooks and Corey, 1964; Brutsaert, 1967; Jones and Wagenet, 1984].

SATURN assumes the following relationship between relative hydraulic conductivity, k_r, and dimensionless moisture content, $\hat{\Theta}$:

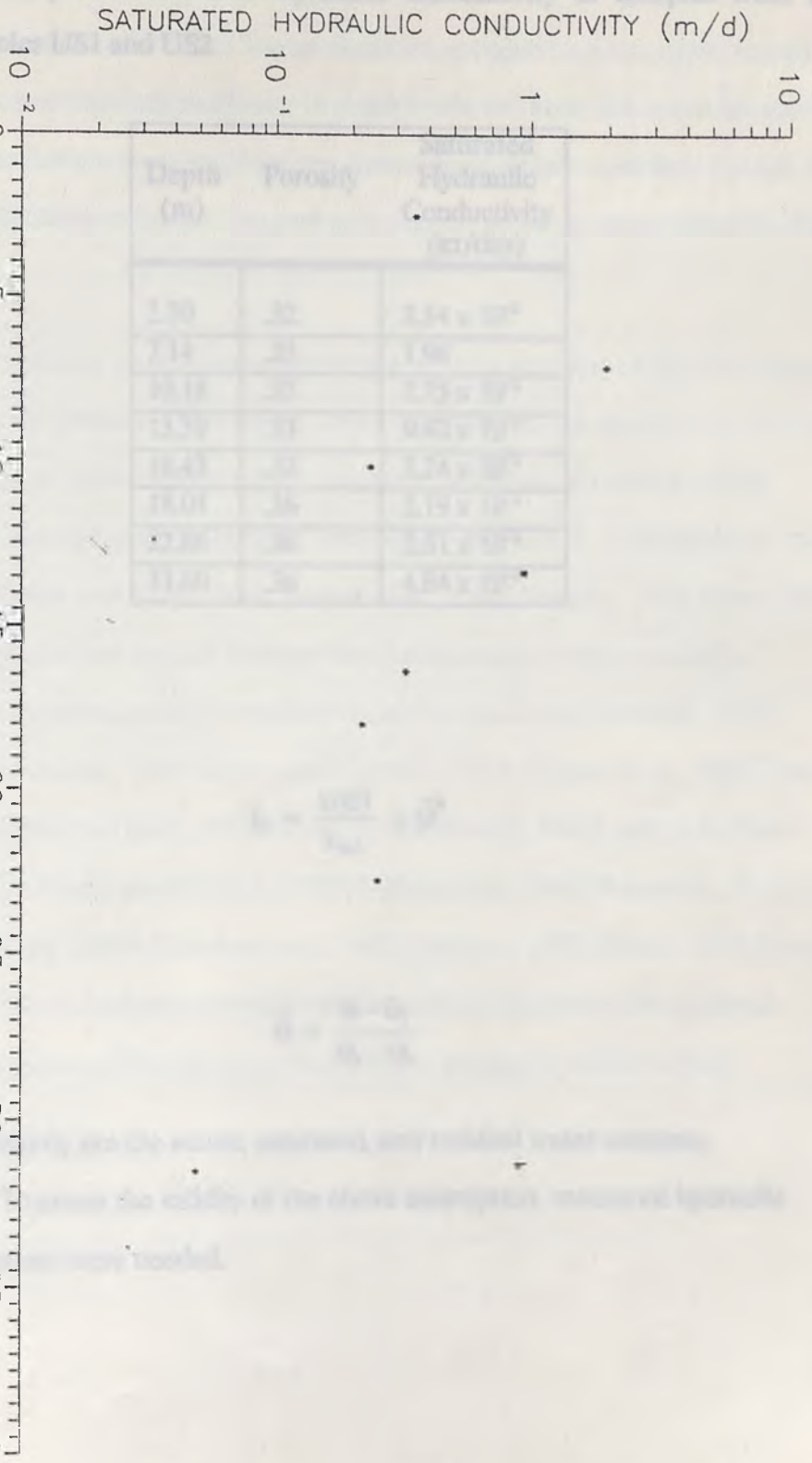

Figure 11 Results of permeameter tests on cores from US1 and US2.

TABLE 1. Porosity and Saturated Hydraulic Conductivity of Samples from Drill Holes US1 and US2

Depth (m)	Porosity	Saturated Hydraulic Conductivity (m/day)
2.50	.32	3.54×10^{-1}
7.14	.33	1.96
10.18	.33	2.35×10^{-1}
13.39	.33	9.42×10^{-1}
16.43	.33	3.24×10^{-1}
18.04	.36	2.19×10^{-1}
22.86	.36	2.51×10^{-1}
31.60	.36	4.84×10^{-2}

$$k_r = \frac{k(\Theta)}{k_{sat}} = \hat{\Theta}^n \tag{3}$$

where

$$\hat{\Theta} = \frac{\Theta - \Theta_r}{\Theta_s - \Theta_r} \tag{4}$$

where Θ, Θ_s, and Θ_r are the actual, saturated, and residual water contents, respectively. To assess the validity of the above assumption, measured hydraulic conductivity values were needed.

Klute [1972], surveyed the various methods for measuring the hydraulic conductivity of unsaturated soils. The methods are grouped into two types: steady-state methods, and unsteady methods. In steady-state methods, the hydraulic gradient and volumetric flux are measured in a one dimensional, steady-state flow system. The hydraulic conductivity at the existing moisture content is then obtained from the Darcy equation.

Unsteady methods use the time dependence of some property of the flow system to determine the hydraulic conductivity. These methods can be classified as outflow-inflow methods, or instantaneous profile methods. A variety of outflow-inflow methods have been proposed [Gardner, 1956; Miller and Elrick, 1958; Rijtema, 1959; Kunze, 1962; Bruce and Klute, 1963; Jackson et al., 1963; Doering, 1965; Peek, 1966]. Many investigators have applied forms of the instantaneous profile method to determine unsaturated hydraulic conductivity in the laboratory [Richards, 1953; Watson, 1966; Vachaud, 1967; Weeks and Richards, 1967; Flocher et al., 1968; Cassel et al., 1968; Rogers and Klute, 1971; Vachaud and Thoney, 1971]; and in the field [Richards, 1956; Ogata and Richards, 1957; Nielsen et al., 1962; Rose et al., 1965; Van Bavel et al., 1968a, 1968b; Davidson et al., 1969; Gardner, 1970; Giesel, 1970; Renger et al., 1970]. The instantaneous profile method used to determine the hydraulic conductivity function of the soil at the RNM site is outlined by Hillel [1972].

Instantaneous Profile Test

Introduction Unsaturated hydraulic conductivity as a function of moisture content was determined by the instantaneous profile technique [Hillel, 1972]. This method, based upon monitoring the internal drainage of a soil profile, requires the frequent and simultaneous measurement of moisture content and matric suction. From these measurements, the soil moisture characteristic, and instantaneous head gradients and moisture fluxes can be determined. The hydraulic conductivity is then obtained as the ratio of the flux to the head gradient. The instantaneous profile technique is an unsteady method that, when applied to a field soil, eliminates the problems associated with laboratory techniques, such as compaction or disaggregation of the sample, loss of soil structure, nonrepresentative sampling, or a change in sample orientation. According to Watson [1966], one attraction to this approach is that, unlike steady-state methods, where the dynamic effects present in unsteady flow are assumed to have a negligible effect on the 'steady-state' hydraulic conductivity, the instantaneous profile method determines conductivities at particular instants in time.

Theory Darcy's law for unsaturated vertical flow can be written as:

$$q = -K(\Theta) \frac{\partial H}{\partial z} \tag{5}$$

where q is the fluid flux, $K(\Theta)$ is the unsaturated hydraulic conductivity as a function of moisture content, H is the hydraulic head, and z is the vertical dimension.

The general equation of continuity for flow through porous media is

$$\frac{\partial \Theta}{\partial t} = -\nabla \cdot q \tag{6}$$

where t is time.

For one-dimensional vertical flow, equation (6) can be written

$$\frac{\partial \Theta}{\partial t} = -\frac{\partial q}{\partial z} \tag{7}$$

Thus,

$$\frac{\partial \Theta}{\partial t} = \frac{\partial}{\partial z}[K(\Theta)\frac{\partial H}{\partial z}] \tag{8}$$

Integrating, we obtain

$$\int_0^z \frac{\partial \Theta}{\partial t}\, dz = q = [K(\Theta)\frac{\partial H}{\partial z}]_z \tag{9}$$

The integral can be evaluated from the moisture data, and an instantaneous flux obtained. The hydraulic head gradient is calculated from tensiometer measurements. Finally,

$$K(\Theta) = \frac{q}{\partial H/\partial z} \tag{10}$$

Experimental Design The site selected for the instantaneous profile test is located approximately 50 m northwest of flume 2 (Figure 3). An area of about 3 m x 4 m was excavated to a depth of 15 cm, and was enclosed by a 20 cm soil berm. The plot was designed to be large enough so that only vertical infiltration occurred in the vicinity of the neutron tubes and tensiometers.

Two holes for neutron access tubes were hand augured to a depth of 250 cm. The bottoms of the tubes were stoppered to prevent the entry of water. 5.08 cm I.D. aluminum neutron access tubes were installed and backfilled with a slurry made from the cuttings.

Two tensiometer arrays--five tensiometers each--were installed in the positions shown, with the shallowest tensiometer at 26 cm, the deepest at 214 cm. The porous tips were packed with mud made of fines from the auger cuttings. The holes were then backfilled with a slurry also made from the cuttings. The exposed tubing and gauges were covered with thick fiberglass insulation to prevent freezing.

A single temperature probe was installed at the position indicated, at a depth of 60 cm to detect the advancing wetting front. A staff gauge was placed in the plot for water depth measurement. Figure 12 shows the locations of the instruments at the test plot.

Two outflow tubes were installed on the southeast corner of the plot to prevent erosion of the berm when the inflow exceeded the infiltration rate during the initial wetting of the profile. An inflow tube was positioned near the center of the plot with a slotted PVC diffuser attached to the end to prevent scour of the plot bottom.

Data Collection Prior to flooding the plot, both neutron tubes were logged at 1 foot intervals and all tensiometer readings were recorded. Water for the test was pumped from the RNM canal to the plot, a distance of about 40 m. By keeping the inflow slightly greater than the infiltration rate, a constant head of approximately 10 cm was maintained at the level of the outflow tubes. Soil moisture and matric suction were monitored to determine when the entire profile was saturated.

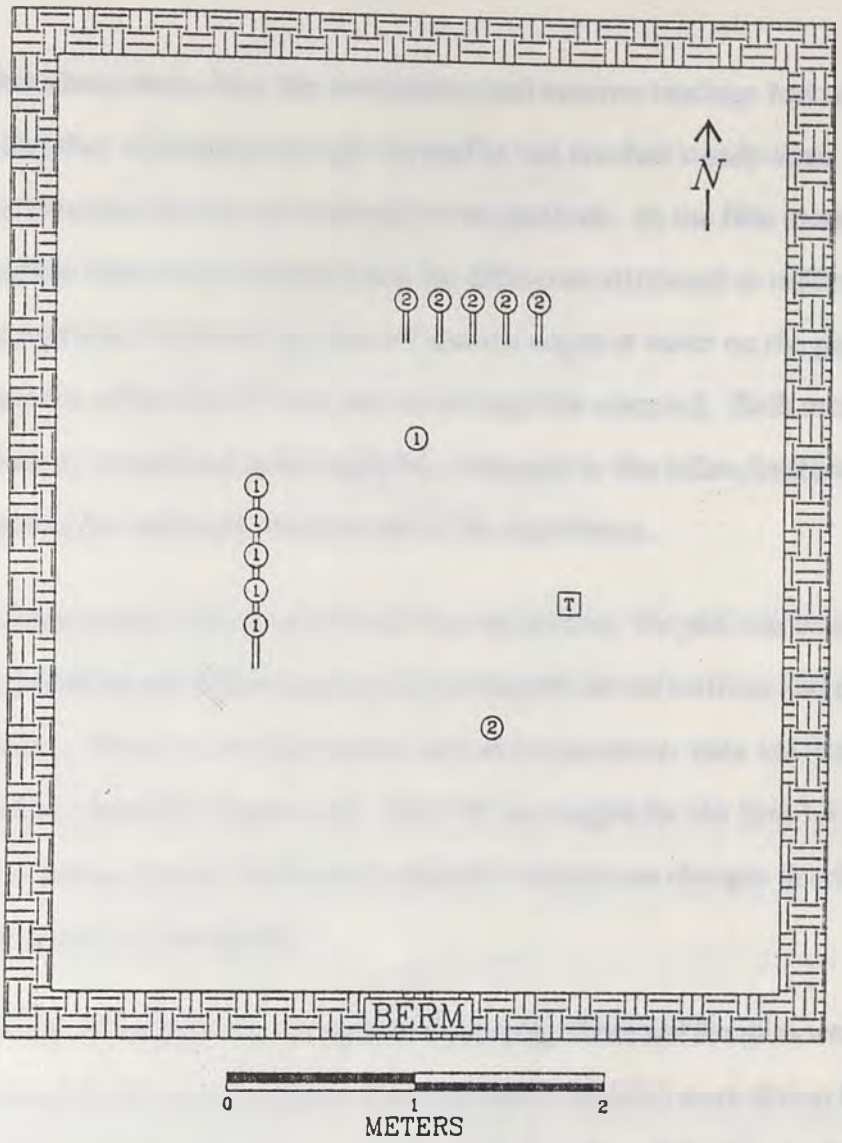

Figure 12. Instantaneous Profile Test Site

After about three days, the tensiometer and neutron readings had stabilized, indicating that infiltration through the profile had reached steady-state. The steady-state infiltration rate was determined by two methods. In the first method, the inflow and outflow rates were measured and the difference attributed to infiltration. In the second method, the pump was shut off and the depth of water on the plot was measured as a function of time, and an average flux obtained. Both methods ignore evaporation, considered to be negligible compared to the inflow/outflow rates and considering the relatively short period of the experiment.

As soon as the water level reached the soil surface, the plot was covered with black plastic and frequent and concurrent measurements of soil wetness and matric suction were taken. Neutron moisture meter data and tensiometer data are listed in Appendices A and B, respectively. Only N1 was logged for the first 1.5 hr. The time between measurements increased as the plot drained and changes in soil moisture and suction occurred less rapidly.

Twenty-three days after cessation of pumping, three soil samples were taken for calibration of the neutron probe. Core barrels (5 cm I.D.) were driven from 50 cm to 60 cm below the plot bottom at a distance of 15 cm from N2. N2 was then logged at this interval.

In Situ Saturated Hydraulic Conductivity Determination After the neutron and tensiometer readings had stabilized, inflow and outflow were measured to determine the infiltration flux. Three measurements at the inflow tube, and three at each outflow tube were made and are listed in Appendix C. The measurements at each

tube were averaged and the flux of infiltration computed as

$$q = \frac{\overline{I} - \overline{O}_1 - \overline{O}_2}{A} \tag{11}$$

$$= \frac{(8.914 \times 10^2 \frac{cm^3}{sec}) - (3.709 \times 10^2 \frac{cm^3}{sec}) - (1.495 \times 10^2 \frac{cm^3}{sec})}{1.93 \times 10^5 \ cm^2}$$

$$= 1.92 \times 10^{-3} \frac{cm}{sec}$$

where q is the infiltration flux (neglecting evaporation), $\overline{I}$ is the average inflow, $\overline{O}_1$ is the average outflow at tube 1, $\overline{O}_2$ is the average outflow at tube 2, and A is the area of the plot.

A second measurement of the infiltration flux was made by recording the rate at which the water level dropped on the plot after the pump was turned off (data are listed in Appendix C). The water level dropped 4.27 cm in 3540 seconds for an average flux of 1.21×10^{-3} cm/sec, again ignoring evaporation.

For saturated vertical flow in a free-draining medium, if the ponding depth is negligible, a unit hydraulic gradient will exist, and the fluid flux will equal the saturated hydraulic conductivity [Black et al., 1969; Davidson et al., 1969; Hillel, 1971]. As can be seen by Figure 13, the infiltration rate is independent of the depth of ponding, which can be considered negligible, and the infiltration fluxes can be used as estimates of the saturated hydraulic conductivity. Conductivities thus obtained agree fairly well with values from other methods (Table 2).

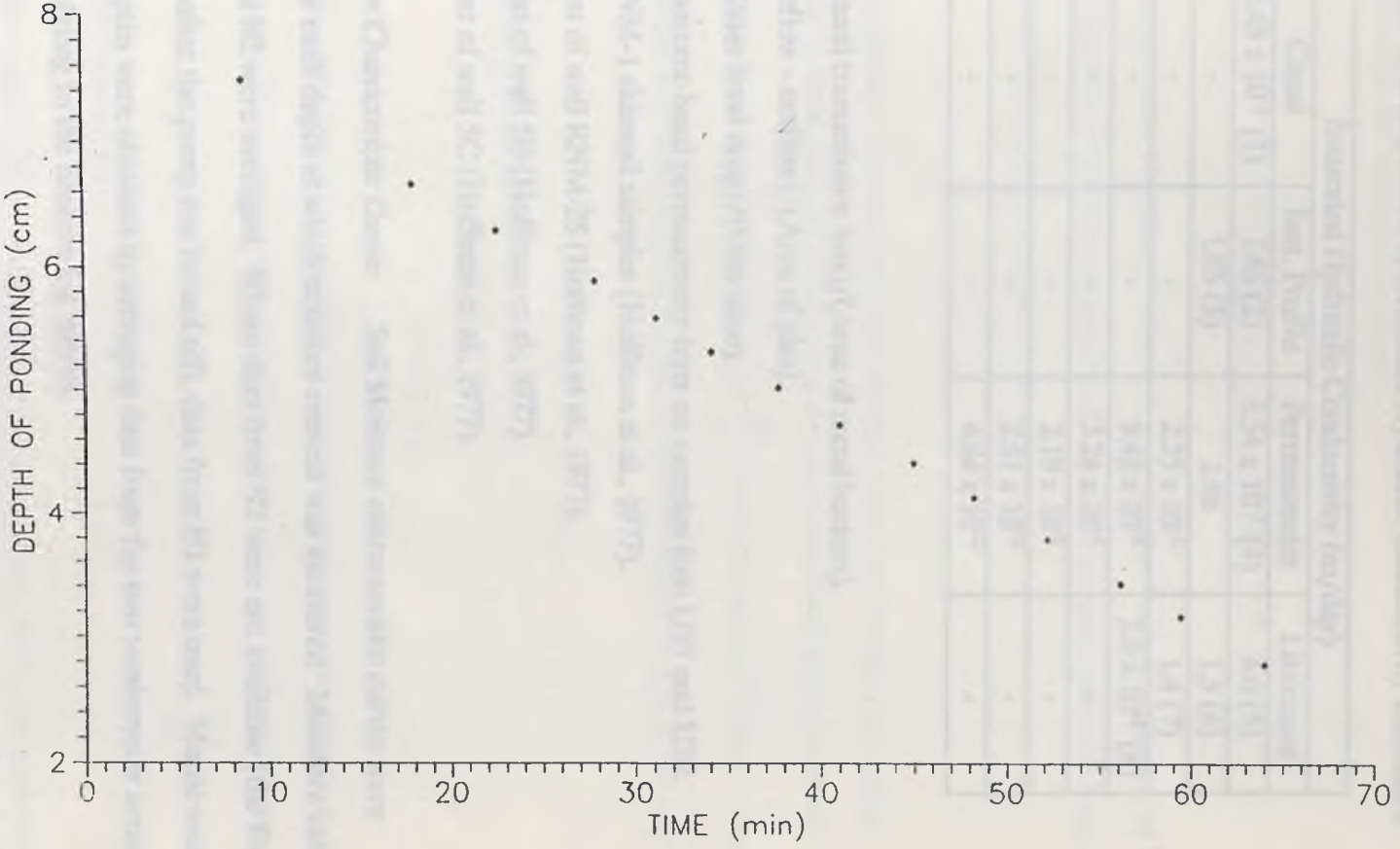

Figure 13. Depth of ponding vs time.

TABLE 2. Comparison of Saturated Hydraulic Conductivity Estimates

Saturated Hydraulic Conductivity (m/day)			
Canal	Inst. Profile	Permeameter	Literature
5.43×10^{-1} (1)	1.66 (2)	3.54×10^{-1} (4)	4.0 (5)
-	1.05 (3)	1.96	1.5 (6)
-	-	2.35×10^{-1}	1.4 (7)
-	-	9.42×10^{-1}	2.0×10^{-1} (8)
-	-	3.24×10^{-1}	-
-	-	2.19×10^{-1}	-
-	-	2.51×10^{-1}	-
-	-	4.84×10^{-2}	-

1. (Canal transmission loss)/(Area of canal bottom).
2. (Inflow - outflow)/(Area of plot).
3. (Water level drop)/(Unit time).
4. Constant-head permeameter tests on samples fron US1 and US2.
5. RNM-1 sidewall samples (Hoffman et al., 1977).
6. Test of well RNM-2S (Hoffman et al., 1977).
7. Test of well 5B (Hoffman et al., 1977).
8. Test of well 5C (Hoffman et al., 1977).

Soil Moisture Characteristic Curves Soil Moisture characteristic curves were produced for each depth at which moisture content was measured. Moisture values from N1 and N2 were averaged. Where data from N2 were not available (the first three hours after the pump was turned off), data from N1 were used. Matric suctions for these depths were obtained by averaging data from the two tensiometer arrays and then interpolating to the neutron log depths.

The curves indicate considerable variability in hydraulic properties with depth. A non-linear least squares curve fitting algorithm [van Genuchten, 1978] was used to

obtain equations for the curves of the form:

$$\Theta = (n - \Theta_r)\left\{\frac{1}{1 + (\alpha \mid \psi - \psi_a \mid)^{\beta}}\right\}^{\gamma} + \Theta_r \qquad (12)$$

where Θ is the moisture content, α, β, and γ are parameters to be determined by the curve fitting algorithm, ψ is the pressure head, ψ_a is the air entry pressure head, n is the porosity, and Θ_r is the residual moisture content.

Unsaturated Hydraulic Conductivity Determination The flux through each depth increment (dz) is determined by integrating the moisture versus time curve with respect to depth (Tables 3 and 4). Values of $\frac{\partial \Theta}{\partial t}$ were obtained by fitting a smooth curve to the data and measuring the tangents to the curves at t = 1, 2, 5, 10, and 20 days.

The total head is calculated as

$$H = \overline{\Psi} + z$$

where $\overline{\Psi}$ is the average matric suction of the two tensiometer arrays. Matric suctions at 1, 2, 5, 10, and 20 days were interpolated from data taken at times which were, in part, determined by technician availability. The hydraulic gradients, $\frac{\partial H}{\partial z}$, are obtained from these plots.

Hydraulic conductivity as a function of moisture content , $K(\Theta)$, for each depth are calculated by dividing the fluxes by the corresponding hydraulic gradient (Tables 5 and 6). Figures 14 and 15 are plots of $K(\Theta)$ versus Θ, for N1 and N2, respectively.

TABLE 3. Calculation of Soil Moisture Flux--N1 (instantaneous profile test)

Time (days)	z (cm)	$\frac{\partial\Theta}{\partial t}$ (hr^{-1})	$dz(\frac{\partial\Theta}{\partial t})$ (cm/hrs)	$q = \sum dz(\frac{\partial\Theta}{\partial t})$ (cm/hrs)
1 day	0-15	7.55×10^{-4}	1.13×10^{-2}	1.13×10^{-2}
	15-45	7.55×10^{-4}	2.26×10^{-2}	3.40×10^{-2}
	45-75	1.39×10^{-3}	4.18×10^{-2}	7.58×10^{-2}
	75-105	6.16×10^{-4}	1.85×10^{-2}	9.42×10^{-2}
	105-135	1.09×10^{-3}	3.26×10^{-2}	1.27×10^{-1}
	135-165	1.01×10^{-3}	3.02×10^{-2}	1.57×10^{-1}
	165-195	1.36×10^{-3}	4.08×10^{-2}	1.98×10^{-1}
2 days	0-15	2.59×10^{-4}	3.88×10^{-3}	3.88×10^{-3}
	15-45	2.59×10^{-4}	7.77×10^{-3}	1.17×10^{-2}
	45-75	4.00×10^{-4}	1.20×10^{-2}	2.37×10^{-2}
	75-105	3.35×10^{-4}	1.01×10^{-2}	3.37×10^{-2}
	105-135	6.95×10^{-4}	2.09×10^{-2}	5.46×10^{-2}
	135-165	3.68×10^{-4}	1.10×10^{-2}	6.56×10^{-2}
	165-195	5.11×10^{-4}	1.53×10^{-2}	8.09×10^{-2}
5 days	0-15	1.57×10^{-4}	2.36×10^{-3}	2.36×10^{-3}
	15-45	1.57×10^{-4}	4.72×10^{-3}	7.08×10^{-3}
	45-75	1.50×10^{-4}	4.50×10^{-3}	1.16×10^{-2}
	75-105	1.17×10^{-4}	3.51×10^{-3}	1.51×10^{-2}
	105-135	3.98×10^{-4}	1.19×10^{-2}	2.70×10^{-2}
	135-165	2.33×10^{-4}	6.98×10^{-3}	3.40×10^{-2}
	165-195	1.75×10^{-4}	5.25×10^{-3}	3.93×10^{-2}
10 days	0-15	1.70×10^{-5}	2.50×10^{-4}	2.50×10^{-4}
	15-45	1.70×10^{-5}	5.00×10^{-4}	7.50×10^{-4}
	45-75	5.80×10^{-5}	1.75×10^{-3}	2.50×10^{-3}
	75-105	6.70×10^{-5}	2.00×10^{-3}	4.50×10^{-3}
	105-135	2.10×10^{-5}	6.25×10^{-4}	5.12×10^{-3}
	135-165	3.30×10^{-5}	1.00×10^{-3}	6.12×10^{-3}
	165-195	5.80×10^{-5}	1.75×10^{-3}	7.88×10^{-3}
20 days	0-15	0.	0.	0.
	15-45	0.	0.	0.
	45-75	0.	0.	0.
	75-105	1.10×10^{-5}	3.13×10^{-4}	3.13×10^{-4}
	150-135	6.00×10^{-6}	1.88×10^{-4}	5.00×10^{-4}
	135-165	0.	0.	5.00×10^{-4}
	165-195	3.10×10^{-5}	9.37×10^{-4}	1.44×10^{-3}

TABLE 4. Calculation of Soil Moisture Flux--N2 (instantaneous profile test)

Time (days)	z (cm)	$\frac{\partial\Theta}{\partial t}$ (hr^{-1})	$dz(\frac{\partial\Theta}{\partial t})$ (cm/hrs)	$q = \sum dz(\frac{\partial\Theta}{\partial t})$ (cm/hrs)
1 day	0-15	1.75×10^{-3}	2.63×10^{-2}	2.63×10^{-2}
	15-45	1.75×10^{-3}	5.25×10^{-2}	7.88×10^{-2}
	45-75	2.09×10^{-3}	6.27×10^{-2}	1.42×10^{-1}
	75-105	1.39×10^{-3}	4.18×10^{-2}	1.83×10^{-1}
	105-135	1.04×10^{-3}	3.12×10^{-2}	2.15×10^{-1}
	135-165	1.16×10^{-3}	3.47×10^{-2}	2.49×10^{-1}
	165-195	1.18×10^{-3}	3.54×10^{-2}	2.85×10^{-1}
2 days	0-15	6.71×10^{-4}	1.01×10^{-2}	1.01×10^{-2}
	15-45	6.71×10^{-4}	2.01×10^{-2}	3.02×10^{-2}
	45-75	5.90×10^{-4}	1.77×10^{-2}	4.79×10^{-2}
	75-105	8.48×10^{-4}	2.54×10^{-2}	7.33×10^{-2}
	105-135	4.47×10^{-4}	1.34×10^{-2}	8.68×10^{-2}
	135-165	6.25×10^{-4}	1.88×10^{-2}	1.06×10^{-1}
	165-195	5.94×10^{-4}	1.78×10^{-2}	1.23×10^{-1}
5 days	0-15	9.40×10^{-5}	1.41×10^{-3}	1.41×10^{-3}
	15-45	9.40×10^{-5}	2.81×10^{-3}	4.22×10^{-3}
	45-75	1.58×10^{-4}	4.75×10^{-3}	8.97×10^{-3}
	75-105	1.15×10^{-4}	3.44×10^{-3}	1.24×10^{-2}
	105-135	7.10×10^{-5}	2.12×10^{-3}	1.45×10^{-2}
	135-165	2.90×10^{-5}	8.75×10^{-4}	1.54×10^{-2}
	165-195	9.21×10^{-5}	2.75×10^{-3}	1.82×10^{-2}
10 days	0-15	4.60×10^{-5}	6.87×10^{-4}	6.87×10^{-4}
	15-45	4.60×10^{-5}	1.38×10^{-3}	2.06×10^{-3}
	45-75	6.20×10^{-5}	1.88×10^{-3}	3.94×10^{-3}
	75-105	1.90×10^{-5}	5.62×10^{-4}	4.50×10^{-3}
	105-135	7.10×10^{-5}	2.12×10^{-3}	6.62×10^{-3}
	135-165	2.90×10^{-5}	8.75×10^{-4}	7.50×10^{-3}
	165-195	4.00×10^{-5}	1.19×10^{-3}	8.69×10^{-3}
20 days	0-15	0.	0.	0.
	15-45	0.	0.	0.
	45-75	2.70×10^{-5}	8.12×10^{-4}	8.12×10^{-4}
	75-105	4.00×10^{-6}	1.25×10^{-4}	9.37×10^{-4}
	105-135	0.	0.	9.37×10^{-4}
	135-165	2.90×10^{-5}	8.75×10^{-4}	1.81×10^{-3}
	165-195	4.00×10^{-5}	1.19×10^{-3}	3.00×10^{-3}

TABLE 5. Calculation of Hydraulic Conductivity--N1 (instantaneous profile test)

z (cm)	q (cm/hr)	$\frac{\partial H}{\partial z}$ (cm/cm)	K (cm/hr)	Θ (%)
15	1.13×10^{-2}	0.50	2.26×10^{-2}	18.80
	2.36×10^{-3}	0.26	9.08×10^{-3}	16.70
	2.50×10^{-4}	0.65	3.80×10^{-4}	15.80
45	3.40×10^{-2}	0.50	6.79×10^{-2}	18.80
	7.08×10^{-3}	0.26	2.72×10^{-2}	16.70
	7.50×10^{-4}	0.65	1.15×10^{-3}	15.80
75	7.58×10^{-2}	0.48	1.58×10^{-1}	22.50
	2.37×10^{-2}	0.40	5.91×10^{-2}	20.70
	1.16×10^{-2}	0.40	2.90×10^{-2}	19.20
	2.50×10^{-3}	0.31	8.06×10^{-3}	18.10
105	9.42×10^{-2}	0.51	1.85×10^{-1}	21.30
	3.37×10^{-2}	0.75	4.49×10^{-2}	19.80
	1.51×10^{-2}	0.45	3.35×10^{-2}	18.50
	4.50×10^{-3}	0.41	1.10×10^{-2}	17.50
	3.13×10^{-4}	0.19	1.65×10^{-3}	16.70
135	1.27×10^{-1}	0.77	1.65×10^{-1}	14.40
	5.46×10^{-2}	0.87	6.26×10^{-2}	13.40
	2.70×10^{-2}	0.81	3.34×10^{-2}	12.00
	5.12×10^{-3}	0.76	6.74×10^{-3}	11.20
	5.00×10^{-4}	0.75	6.70×10^{-4}	10.90
165	1.57×10^{-1}	0.77	2.04×10^{-1}	12.70
	6.56×10^{-2}	0.87	7.54×10^{-2}	12.20
	3.40×10^{-2}	0.81	4.20×10^{-2}	11.60
	6.12×10^{-3}	0.76	8.06×10^{-3}	10.90
	5.00×10^{-4}	0.75	6.70×10^{-4}	10.90
195	1.98×10^{-1}	0.77	2.57×10^{-1}	18.60
	8.09×10^{-2}	0.87	9.30×10^{-2}	17.90
	3.93×10^{-2}	0.81	4.85×10^{-2}	16.60
	7.88×10^{-3}	0.76	1.04×10^{-2}	15.50
	1.44×10^{-3}	0.75	1.92×10^{-3}	14.80

TABLE 6. Calculation of Hydraulic Conductivity--N2 (instantaneous profile test)

z (cm)	q (cm/hr)	$\frac{\partial H}{\partial z}$ (cm/cm)	K (cm/hr)	Θ (%)
15	2.63×10^{-2}	0.50	5.26×10^{-2}	19.30
	1.41×10^{-3}	0.26	5.41×10^{-3}	16.10
	6.87×10^{-4}	0.65	1.06×10^{-3}	15.60
45	7.88×10^{-2}	0.50	1.58×10^{-1}	19.30
	4.22×10^{-3}	0.26	1.62×10^{-2}	16.10
	2.06×10^{-3}	0.65	3.17×10^{-3}	15.60
75	1.42×10^{-1}	0.48	2.95×10^{-1}	22.50
	4.79×10^{-2}	0.40	1.20×10^{-1}	20.90
	8.97×10^{-3}	0.40	2.24×10^{-2}	19.10
	3.94×10^{-3}	0.31	1.27×10^{-2}	17.80
	8.12×10^{-4}	0.42	1.93×10^{-3}	16.90
105	1.83×10^{-1}	0.51	3.96×10^{-1}	20.40
	7.33×10^{-2}	0.75	9.78×10^{-2}	18.80
	1.24×10^{-2}	0.45	2.76×10^{-2}	17.60
	4.50×10^{-3}	0.41	1.10×10^{-2}	17.00
	9.37×10^{-4}	0.19	4.93×10^{-3}	16.70
135	2.15×10^{-1}	0.77	2.79×10^{-1}	16.50
	8.68×10^{-2}	0.87	9.97×10^{-2}	15.00
	1.45×10^{-2}	0.81	1.79×10^{-2}	14.60
	6.62×10^{-3}	0.76	8.72×10^{-3}	13.80
	9.37×10^{-4}	0.75	1.25×10^{-3}	13.20
165	2.49×10^{-1}	0.77	3.24×10^{-1}	17.30
	1.06×10^{-1}	0.87	1.21×10^{-1}	15.90
	1.54×10^{-2}	0.81	1.90×10^{-2}	15.20
	7.50×10^{-3}	0.76	9.87×10^{-3}	14.60
	1.81×10^{-3}	0.75	2.42×10^{-3}	14.10
195	2.85×10^{-1}	0.77	3.70×10^{-1}	19.70
	1.23×10^{-1}	0.87	1.42×10^{-1}	18.50
	1.82×10^{-2}	0.81	2.42×10^{-2}	18.00
	8.69×10^{-3}	0.76	1.43×10^{-2}	17.00
	3.00×10^{-3}	0.75	4.00×10^{-3}	16.10

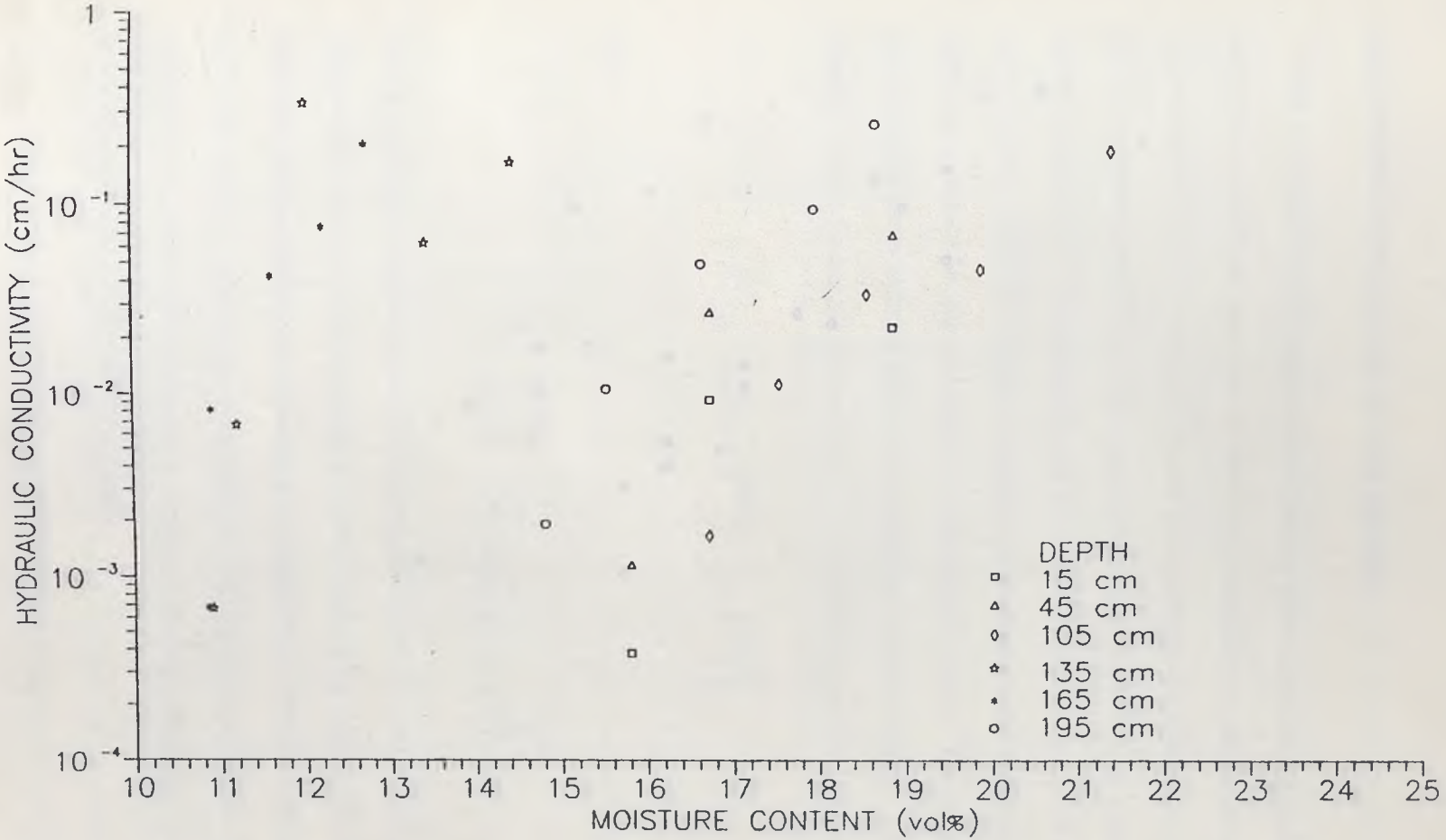

Figure 14. Hydraulic conductivity vs moisture content, Hole N1.

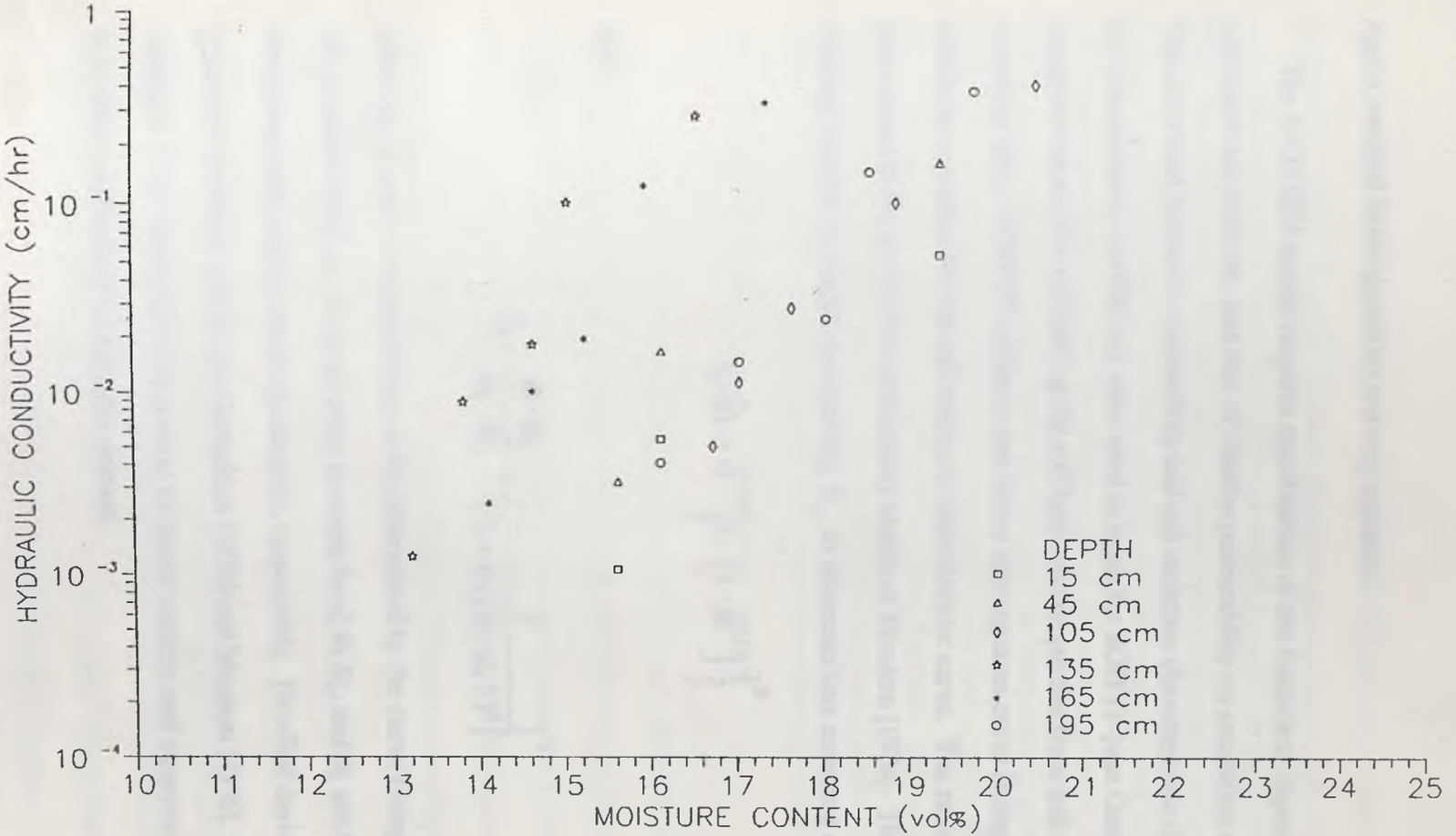

Figure 15. Hydraulic conductivity vs moisture content, Hole N2.

Again, vertical heterogeneities are very apparent.

The SATURN model requires specification of the functional dependence of saturation on pressure, and that of relative permeability on saturation or pressure. The saturated hydraulic conductivity and soil moisture characteristic data obtained in the instantaneous profile test were used as input for SOHYP [van Genuchten, 1978], a computer model for calculating the soil hydraulic properties from soil moisture retention data. SOHYP utilizes a non linear least squares curve fitting algorithm to obtain an equation for the soil moisture characteristic curve. The resulting equation is substituted in the predictive conductivity model of Mualem [1976]. The equation relating relative hydraulic conductivity, K_r, to dimensionless moisture content, $\hat{\Theta}$,is

$$k_r(\hat{\Theta}) = \hat{\Theta}^{1/2}\left\{1 - \left(1 - \hat{\Theta}^{1/\gamma}\right)^{\gamma}\right\}^2 \qquad (13)$$

and

$$\hat{\Theta} = \frac{\Theta - \Theta_r}{\Theta_s - \Theta_r} = \left\{\frac{1}{1 + (\alpha \mid \psi - \psi_a \mid)^{\beta}}\right\}^{\gamma} \qquad (14)$$

where α, β, and γ are parameters to be determined by the curve fitting algorithm, ψ is the pressure head, ψ_a is the air entry pressure head, Θ, Θ_s, and Θ_r are the actual, saturated, and residual moisture contents, respectively. Detailed derivations of these equations can be found in van Genuchten [1978] and Mualem [1976]. SATURN uses equation 14 to relate moisture content to matric suction, and equation 3 to relate hydraulic conductivity to moisture content.

The range of moisture values observed in the instantaneous profile test was fairly small: 12% - 33%. To aid in the curve fitting process, a point at the dry, high tension end of the curve, was taken from NTS soil moisture retention data assembled by Romney, et al [1973]. The data selected were from a soil sample collected 3 km. southwest of the RNM site at approximately the same elevation on Frenchman Flat as the instantaneous profile test site. Since most of the transport in this study occurred at relatively high moisture contents, the shape of the characteristic curve at high tensions should have little affect on the numerical solutions of SATURN. Although the water retention curve fit was consistently good, hydraulic conductivity curves generated with equation 13 generally matched the field data poorly. The slopes of the generated curves are consistently less than the slopes of lines fit to the field data, regardless of the choice of n.

One possible solution to this problem would be to use a different function to relate hydraulic conductivity to saturation. Many such equations can be found in the literature [Sisson et al., 1980; Mualem,1976]. However, only the binary code was available for use in this investigation making any program modifications not possible. Table 7 lists the SATURN input requirements, and the values used for the canal simulations.

Model Definition

The original solution domain was a rectangular grid in the x-z plane consisting of 551 rectangular elements defined by 600 nodes (Figure 16). Only one side of the canal was modeled, exploiting the symmetry of the flow system. The grid extended to a depth of 270 m (50 meters below the water table) and to a distance of 1000 m in the

TABLE 7. RNM Canal Model Input Data

Parameter	Value
Number of nodes	780
Number of elements	711
Time step type	Central difference
Saturated hydraulic conductivity component K_{xx}, material 1	.543 m/day
Saturated hydraulic conductivity component K_{zz}, material 1	.543 m/day
Saturated hydraulic conductivity component K_{xz}, material 1	0 m/day
Saturated hydraulic conductivity component K_{xx}, material 2	5.43 m/day
Saturated hydraulic conductivity component K_{zz}, material 2	.543 m/day
Saturated hydraulic conductivity component K_{xz}, material 2	0 m/day
Effective porosity	.33
Residual water phase saturation	.284
Functional coefficient n (1)	4.0
Functional coefficient α (2)	.0181
Functional coefficient β (2)	2.36
Functional coefficient γ (2)	.577
Decay coefficient	1.55×10^{-4} day^{-1}
Retardation coefficient, R_o	.8
Longitudinal dispersivity, α_L	10 m
Transverse dispersivity, α_T	3 m
Molecular diffusion component, D°_{xx}	1.0×10^{-7} m^2/day
Molecular diffusion component, D°_{zz}	1.0×10^{-7} m^2/day

(1). $$K_{rw} = \frac{(S_w - S_{wr})^n}{(1 - S_{wr})^n}$$

(2). $$S_w - S_{wr} = \frac{(1 - S_{wr})}{[1 + (\alpha \mid \psi - \psi_a \mid)^{\beta}]^{\gamma}}$$

NODES

20	40	60	80	100	120	140	160	180	200	220	240	260	280	300	320	340	360	380	400	420	440	460	480	500	520	540	560	580	600
19	39	59	79	99	119	139	159	179	199	219	239	259	279	299	319	339	359	379	399	419	439	459	479	499	519	539	559	579	599
18	38	58	78	98	118	138	158	178	198	218	238	258	278	298	318	338	358	378	398	418	438	458	478	498	518	538	558	578	598
17	37	57	77	97	117	137	157	177	197	217	237	257	277	297	317	337	357	377	397	417	437	457	477	497	517	537	557	577	597
16	36	56	76	96	116	136	156	176	196	216	236	256	276	296	316	336	356	376	396	416	436	456	476	496	516	536	556	576	596
15	35	55	75	95	115	135	155	175	195	215	235	255	275	295	315	335	355	375	395	415	435	455	475	495	515	535	555	575	595
14	34	54	74	94	114	134	154	174	194	214	234	254	274	294	314	334	354	374	394	414	434	454	474	494	514	534	554	574	594
13	33	53	73	93	113	133	153	173	193	213	233	253	273	293	313	333	353	373	393	413	433	453	473	493	513	533	553	573	593
12	32	52	72	92	112	132	152	172	192	212	232	252	272	292	312	332	352	372	392	412	432	452	472	492	512	532	552	572	592
11	31	51	71	91	111	131	151	171	191	211	231	251	271	291	311	331	351	371	391	411	431	451	471	491	511	531	551	571	591
10	30	50	70	90	110	130	150	170	190	210	230	250	270	290	310	330	350	370	390	410	430	450	470	490	510	530	550	570	590
9	29	49	69	89	109	129	149	169	189	209	229	249	269	289	309	329	349	369	389	409	429	449	469	489	509	529	549	569	589
8	28	48	68	88	108	128	148	168	188	208	228	248	268	288	308	328	348	368	388	408	428	448	468	488	508	528	548	568	588
7	27	47	67	87	107	127	147	167	187	207	227	247	267	287	307	327	347	367	387	407	427	447	467	487	507	527	547	567	587
6	26	46	66	86	106	126	146	166	186	206	226	246	266	286	306	326	346	366	386	406	426	446	466	486	506	526	546	566	586
5	25	45	65	85	105	125	145	165	185	205	225	245	265	285	305	325	345	365	385	405	425	445	465	485	505	525	545	565	585
4	24	44	64	84	104	124	144	164	184	204	224	244	264	284	304	324	344	364	384	404	424	444	464	484	504	524	544	564	584
3	23	43	63	83	103	123	143	163	183	203	223	243	263	283	303	323	343	363	383	403	423	443	463	483	503	523	543	563	583
2	22	42	62	82	102	122	142	162	182	202	222	242	262	282	302	322	342	362	382	402	422	442	462	482	502	522	542	562	582
1	21	41	61	81	101	121	141	161	181	201	221	241	261	281	301	321	341	361	381	401	421	441	461	481	501	521	541	561	581

ELEMENTS

19	38	57	76	95	114	133	152	171	190	209	228	247	266	285	304	323	342	361	380	399	418	437	456	475	494	513	532	551	
18	37	56	75	94	113	132	151	170	189	208	227	246	265	284	303	322	341	360	379	398	417	436	455	474	493	512	531	550	
17	36	55	74	93	112	131	150	169	188	207	226	245	264	283	302	321	340	359	378	397	416	435	454	473	492	511	530	549	
16	35	54	73	92	111	130	149	168	187	206	225	244	263	282	301	320	339	358	377	396	415	434	453	472	491	510	529	548	
15	34	53	72	91	110	129	148	167	186	205	224	243	262	281	300	319	338	357	376	395	414	433	452	471	490	509	528	547	
14	33	52	71	90	109	128	147	166	185	204	223	242	261	280	299	318	337	356	375	394	413	432	451	470	489	508	527	546	
13	32	51	70	89	108	127	146	165	184	203	222	241	260	279	298	317	336	355	374	393	412	431	450	469	488	507	526	545	
12	31	50	69	88	107	126	145	164	183	202	221	240	259	278	297	316	335	354	373	392	411	430	449	468	487	506	525	544	
11	30	49	68	87	106	125	144	163	182	201	220	239	258	277	296	315	334	353	372	391	410	429	448	467	486	505	524	543	
10	29	48	67	86	105	124	143	162	181	200	219	238	257	276	295	314	333	352	371	390	409	428	447	466	485	504	523	542	
9	28	47	66	85	104	123	142	161	180	199	218	237	256	275	294	313	332	351	370	389	408	427	446	465	484	503	522	541	
8	27	46	65	84	103	122	141	160	179	198	217	236	255	274	293	312	331	350	369	388	407	426	445	464	483	502	521	540	
7	26	45	64	83	102	121	140	159	178	197	216	235	254	273	292	311	330	349	368	387	406	425	444	463	482	501	520	539	
6	25	44	63	82	101	120	139	158	177	196	215	234	253	272	291	310	329	348	367	386	405	424	443	462	481	500	519	538	
5	24	43	62	81	100	119	138	157	176	195	214	233	252	271	290	309	328	347	366	385	404	423	442	461	480	499	518	537	
4	23	42	61	80	99	118	137	156	175	194	213	232	251	270	289	308	327	346	365	384	403	422	441	460	479	498	517	536	
3	22	41	60	79	98	117	136	155	174	193	212	231	250	269	288	307	326	345	364	383	402	421	440	459	478	497	516	535	
2	21	40	59	78	97	116	135	154	173	192	211	230	249	268	287	306	325	344	363	382	401	420	439	458	477	496	515	534	
1	20	39	58	77	96	115	134	153	172	191	210	229	248	267	286	305	324	343	362	381	400	419	438	457	476	495	514	533	

Figure 16. Original sample space discretization into nodes and elements.

horizontal direction. Node spacing increased with depth and with horizontal distance from the canal. Element size ranged from .5 m x .5 m at the canal to 50 m x 200 m for elements furthest from the canal.

At the canal, pressure heads were held constant at +20 cm. Initial hydraulic heads at and below the water table were hydrostatic. All other nodes were initially -100 cm (approximately 60% saturated). Although this degree of saturation is unrealistically high, a lower value of initial saturation caused numerical instabilities in the program , and, regardless of the time step size, nonconvergence.

The vertical boundary beneath the canal (x = 0) was treated as a no-flow boundary because of the symmetry of the flow system. Vertical flow through the the lower boundary was ignored , therefore a no flow boundary was assigned at the bottom of the model domain. It was assumed that any groundwater mound that might develop below the canal would not extend 1000 m to the right boundary, thus nodes at and below the water table on the right boundary were held constant at hydrostatic pressure. Assuming only vertical flow in the unsaturated zone at x = 1000 m, the remainder of the right boundary was treated as a no-flow boundary. In light of the low annual precipitation on Frenchman Flat, and ignoring evapotranspiration, the ground surface to the right of the canal was treated as a no-flow boundary.

At the beginning of the simulation, with the wetting front in the small elements, solution convergence was rapid. As the front moved into progressively larger elements, more iterations were required at each time step for convergence. When the vertical spacing of nodes at the wetting front exceeded 10 m, the solution became unstable and the program failed to converge. Decreasing the time step size had little

effect on solution stability. To resolve the problem, a new grid with a maximum node spacing of 10 m was developed.

Execution time required for each iteration is roughly proportional to the number of nodes in the grid. To maintain about the same number of nodes (thereby keeping execution time at a reasonable level), while greatly increasing overall node density, the size of the solution domain had to be reduced. This was accomplished in two ways: the horizontal extent of the grid was reduced from 1000 m to 200 m; and, rather than a rectangular sample space, the upper-right portion of the grid was eliminated, leaving a stair-stepped boundary on the right (Figure 11). The new grid consists of 711 elements and 780 nodes (Figures 17 and 18). As in the original grid, node spacing increased with depth and horizontal distance from the canal; however, in the new grid, node spacing is reduced as the water table is approached . This is to aid in the numerical handling of the wide range of pressures and hydraulic conductivities encountered at the saturated-unsaturated interface. Figure 19 shows the elements (to scale) with the model boundary conditions.

Boundary and initial conditions for the new grid are essentially the same as those for the old grid, with the exception of the initial saturation of the nodes above the water table. These nodes were given a hydrostatic pressure ($\frac{p}{\rho g}$ = - distance above the water table) up to a maximum suction of -100 cm.

DEPTH (m)																																
0	703	704	705	706	707	708	709	710	711																							
.5	694	695	696	697	698	699	700	701	702																							
1.	685	686	687	688	689	690	691	692	693																							
1.5	676	677	678	679	680	681	682	683	684																							
2	667	668	669	670	671	672	673	674	675																							
3	658	659	660	661	662	663	664	665	666																							
4	649	650	651	652	653	654	655	656	657																							
5	636	637	638	639	640	641	642	643	644	645	646	647	648																			
6	623	624	625	626	627	628	629	630	631	632	633	634	635																			
8	610	611	612	613	614	615	616	617	618	619	620	621	622																			
10	597	598	599	600	601	602	603	604	605	606	607	608	609																			
12	584	585	586	587	588	589	590	591	592	593	594	595	596																			
15	571	572	573	574	575	576	577	578	579	580	581	582	583																			
20	558	559	560	561	562	563	564	565	566	567	568	569	570																			
25	541	542	543	544	545	546	547	548	549	550	551	552	553	554	555	556	557															
30	524	525	526	527	528	529	530	531	532	533	534	535	536	537	538	539	540															
35	507	508	509	510	511	512	513	514	515	516	517	518	519	520	521	522	523															
45	490	491	492	493	494	495	496	497	498	499	500	501	502	503	504	505	506															
55	473	474	475	476	477	478	479	480	481	482	483	484	485	486	487	488	489															
65	456	457	458	459	460	461	462	463	464	465	466	467	468	469	470	471	472															
75	439	440	441	442	443	444	445	446	447	448	449	450	451	452	453	454	455															
85	418	419	420	421	422	423	424	425	426	427	428	429	430	431	432	433	434	435	436	437	438											
95	397	398	399	400	401	402	403	404	405	406	407	408	409	410	411	412	413	414	415	416	417											
105	376	377	378	379	380	381	382	383	384	385	386	387	388	389	390	391	392	393	394	395	396											
115	355	356	357	358	359	360	361	362	363	364	365	366	367	368	369	370	371	372	373	374	375											
125	334	335	336	337	338	339	340	341	342	343	344	345	346	347	348	349	350	351	352	353	354											
135	313	314	315	316	317	318	319	320	321	322	323	324	325	326	327	328	329	330	331	332	333											
145	292	293	294	295	296	297	298	299	300	301	302	303	304	305	306	307	308	309	310	311	312											
155	267	268	269	270	271	272	273	274	275	276	277	278	279	280	281	282	283	284	285	286	287	288	289	290	291							
165	242	243	244	245	246	247	248	249	250	251	252	253	254	255	256	257	258	259	260	261	262	263	264	265	266							
175	217	218	219	220	221	222	223	224	225	226	227	228	229	230	231	232	233	234	235	236	237	238	239	240	241							
185	192	193	194	195	196	197	198	199	200	201	202	203	204	205	206	207	208	209	210	211	212	213	214	215	216							
195	167	168	169	170	171	172	173	174	175	176	177	178	179	180	181	182	183	184	185	186	187	188	189	190	191							
205	142	143	144	145	146	147	148	149	150	151	152	153	154	155	156	157	158	159	160	161	162	163	164	165	166							
210	117	118	119	120	121	122	123	124	125	126	127	128	129	130	131	132	133	134	135	136	137	138	139	140	141							
215	88	89	90	91	92	93	94	95	96	97	98	99	100	101	102	103	104	105	106	107	108	109	110	111	112	113	114	115	116			
217	59	60	61	62	63	64	65	66	67	68	69	70	71	72	73	74	75	76	77	78	79	80	81	82	83	84	85	86	87			
219	30	31	32	33	34	35	36	37	38	39	40	41	42	43	44	45	46	47	48	49	50	51	52	53	54	55	56	57	58			
220	1	2	3	4	5	6	7	8	9	10	11	12	13	14	15	16	17	18	19	20	21	22	23	24	25	26	27	28	29			
x(m)	0	.5	1	1.5	2	3	5	7	10	15	20	25	30	40	50	60	70	80	90	100	110	120	130	140	150	160	170	180	190	200		

Figure 17. Location of elements.

DEPTH (m)																														
0	771	772	773	774	775	776	777	778	779	780																				
.5	761	762	763	764	765	766	767	768	769	770																				
1	751	752	753	754	755	756	757	758	759	760																				
1.5	741	742	743	744	745	746	747	748	749	750																				
2	731	732	733	734	735	736	737	738	739	740																				
3	721	722	723	724	725	726	727	728	729	730																				
4	711	712	713	714	715	716	717	718	719	720																				
5	697	698	699	700	701	702	703	704	705	706	707	708	709	710																
6	683	684	685	686	687	688	689	690	691	692	693	694	695	696																
8	669	670	671	672	673	674	675	676	677	678	679	680	681	682																
10	655	656	657	658	659	660	661	662	663	664	665	666	667	668																
12	641	642	643	644	645	646	647	648	649	650	651	652	653	654																
15	627	628	629	630	631	632	633	634	635	636	637	638	639	640																
20	613	614	615	616	617	618	619	620	621	622	623	624	625	626																
25	595	596	597	598	599	600	601	602	603	604	605	606	607	608	609	610	611	612												
30	577	578	579	580	581	582	583	584	585	586	587	588	589	590	591	592	593	594												
35	559	560	561	562	563	564	565	566	567	568	569	570	571	572	573	574	575	576												
45	541	542	543	544	545	546	547	548	549	550	551	552	553	554	555	556	557	558												
55	523	524	525	526	527	528	529	530	531	532	533	534	535	536	537	538	539	540												
65	505	506	507	508	509	510	511	512	513	514	515	516	517	518	519	520	521	522												
75	487	488	489	490	491	492	493	494	495	496	497	498	499	500	501	502	503	504												
85	465	466	467	468	469	470	471	472	473	474	475	476	477	478	479	480	481	482	483	484	485	486								
95	443	444	445	446	447	448	449	450	451	452	453	454	455	456	457	458	459	460	461	462	463	464								
105	421	422	423	424	425	426	427	428	429	430	431	432	433	434	435	436	437	438	439	440	441	442								
115	399	400	401	402	403	404	405	406	407	408	409	410	411	412	413	414	415	416	417	418	419	420								
125	377	378	379	380	381	382	383	384	385	386	387	388	389	390	391	392	393	394	395	396	397	398								
135	355	356	357	358	359	360	361	362	363	364	365	366	367	368	369	370	371	372	373	374	375	376								
145	333	334	335	336	337	338	339	340	341	342	343	344	345	346	347	348	349	350	351	352	353	354								
155	307	308	309	310	311	312	313	314	315	316	317	318	319	320	321	322	323	324	325	326	327	328	329	330	331	332				
165	281	282	283	284	285	286	287	288	289	290	291	292	293	294	295	296	297	298	299	300	301	302	303	304	305	306				
175	255	256	257	258	259	260	261	262	263	264	265	266	267	268	269	270	271	272	273	274	275	276	277	278	279	280				
185	229	230	231	232	233	234	235	236	237	238	239	240	241	242	243	244	245	246	247	248	249	250	251	252	253	254				
195	203	204	205	206	207	208	209	210	211	212	213	214	215	216	217	218	219	220	221	222	223	224	225	226	227	228				
205	177	178	179	180	181	182	183	184	185	186	187	188	189	190	191	192	193	194	195	196	197	198	199	200	201	202				
210	151	152	153	154	155	156	157	158	159	160	161	162	163	164	165	166	167	168	169	170	171	172	173	174	175	176				
215	121	122	123	124	125	126	127	128	129	130	131	132	133	134	135	136	137	138	139	140	141	142	143	144	145	146	147	148	149	150
217	91	92	93	94	95	96	97	98	99	100	101	102	103	104	105	106	107	108	109	110	111	112	113	114	115	116	117	118	119	120
219	61	62	63	64	65	66	67	68	69	70	71	72	73	74	75	76	77	78	79	80	81	82	83	84	85	86	87	88	89	90
220	31	32	33	34	35	36	37	38	39	40	41	42	43	44	45	46	47	48	49	50	51	52	53	54	55	56	57	58	59	60
225	1	2	3	4	5	6	7	8	9	10	11	12	13	14	15	16	17	18	19	20	21	22	23	24	25	26	27	28	29	30
x(m)	0	.5	1	1.5	2	3	5	7	10	15	20	25	30	40	50	60	70	80	90	100	110	120	130	140	150	160	170	180	190	200

Figure 18. Location of nodes.

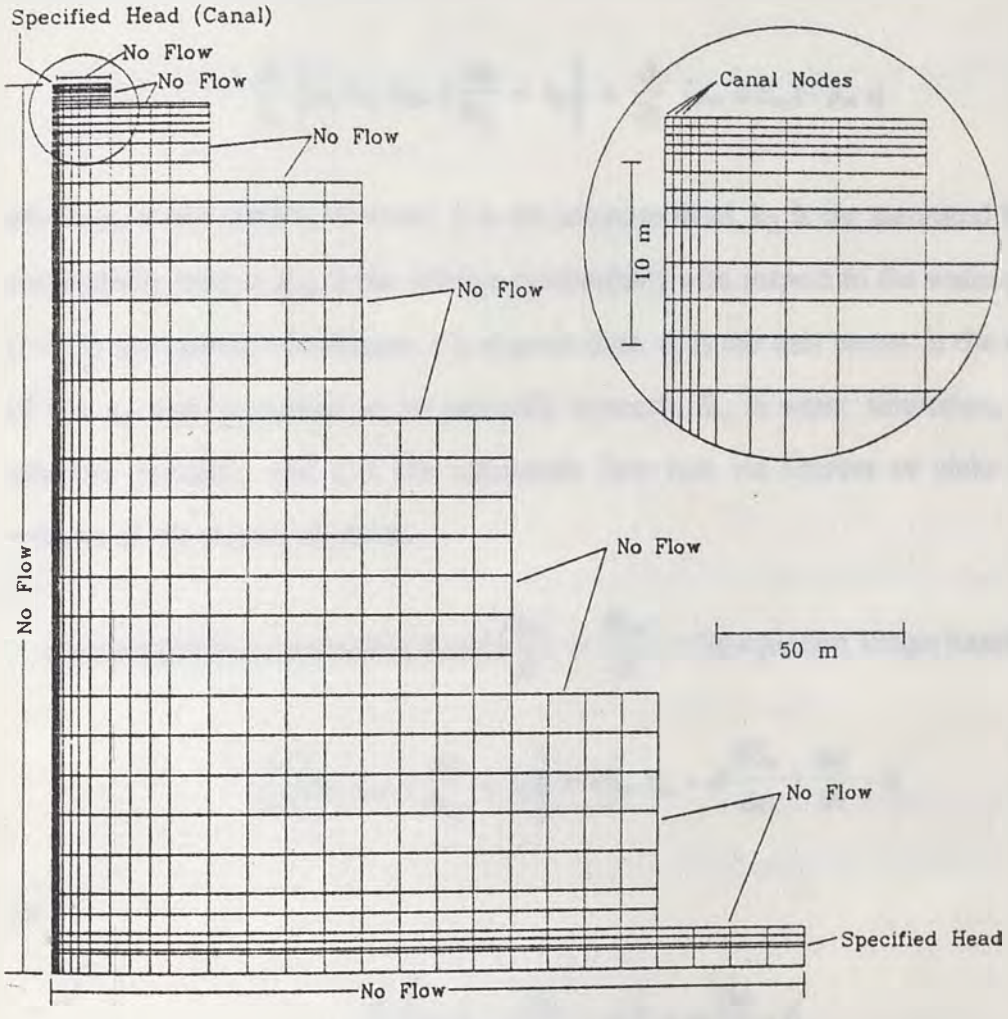

Figure 19. Discretization of sample space showing boundary conditions.

MATHEMATICAL FORMULATION

Governing Equations--Flow

Combination of the continuity equation and Darcy's law written for variably saturated soil in two dimensions yields:

$$\frac{\partial}{x_i}\left\{\rho_w\, k_{ij}\, k_{rw}\,(\frac{\partial\psi}{\partial x_j} + e_j)\right\} = \frac{\partial}{\partial t}\,(\rho_w\,\phi\,S_w) - \rho_w\, q \qquad (15)$$

where ρ_w is the density of water, ψ is the pressure head, k_{ij} is the saturated hydraulic conductivity tensor, k_{rw} is the relative permeability with respect to the water phase, x_i ($i=1,2$) are spatial coordinates, t is elapsed time, e_j is the unit vector in the direction of the x_2 axis (assumed to be vertically upward), S_w is water saturation, ϕ is the effective porosity, and q is the volumetric flow rate via sources or sinks per unit volume of the porous medium.

For a slightly compressible fluid ($\frac{\partial\rho_w}{\partial x} = \frac{\partial\rho_w}{\partial t} = 0$), equation 15 can be written:

$$\frac{\partial}{\partial x_i}\left\{k_{ij}\, k_{rw}\,(\frac{\partial\psi}{\partial x_j} + e_j)\right\} = (S_w\, S_s + \phi\frac{dS_w}{d\psi})\,\frac{\partial\psi}{\partial t} - q \qquad (16)$$

or

$$\frac{\partial}{\partial x_i}\left\{k_{ij}\, k_{rw}\,(\frac{\partial\psi}{\partial x_j} + e_j)\right\} = \eta\,\frac{\partial\psi}{\partial t} - q \qquad (17)$$

where

$$\eta = S_w S_s + \phi \frac{dS_w}{d\psi} \tag{18}$$

and S_s = the specific storage = $\rho_w g (\phi \beta + \alpha)$, where g is the gravitational constant and α and β are coefficients of compressibility of the porous medium and water, respectively.

The boundary and initial conditions of the variably saturated flow problem can be expressed as:

$$\psi(x_i, 0) = \psi_0(x_i) \tag{19}$$

$$\psi(x_i, t) = \hat{\psi} \text{ on } B_1 \tag{20}$$

and

$$v_i n_i = v_n \text{ on } B_2 \tag{21}$$

where ψ_0 is the initial head value, B_1 is the portion of the flow boundary where ψ is prescribed as $\hat{\psi}$, B_2 is the portion of the flow boundary where the outward fluid flux is prescribed as v_n, and n_i is the outward unit normal vector on B_2.

SATURN solves equation 17 by the Galerkin finite element method subject to equations 19 - 21. The Darcy velocity components are then calculated from:

$$q_i = -K_{ij} k_{rw} \left(\frac{\partial \psi}{\partial x_j} + e_j\right) \tag{22}$$

Governing Equations--Transport

The governing equation for two-dimensional transport of a non-conservative solute in a variably saturated medium can be written:

$$\frac{\partial}{\partial x_i}\left(D_{ij}\frac{\partial c}{\partial x_j}\right) - \frac{\partial}{\partial x_i}(v_i\, c) =$$

$$\frac{\partial}{\partial t}\left\{\phi\, S_w\, c + \rho_s\,(1-\phi)\, c_s\right\} - q\, c^* + \lambda\left\{\phi\, S_w\, c + \rho_s\,(1-\phi)\, c_s\right\} \qquad (23)$$

where D_{ij} is the apparent hydrodynamic dispersion tensor, c is the solute concentration in the fluid, v_i is the Darcy velocity, ρ_s is the density of the solid grains, c_s is the adsorbed concentration, λ is the first-order decay coefficient, and c^* is the solute concentration of the injected fluid.

If the adsorbtion relationship can be described by a linear equilibrium isotherm, equation 23 becomes:

$$\frac{\partial}{\partial x_i}\left(D_{ij}\,\frac{\partial c}{\partial x_j}\right) - \frac{\partial}{\partial x_i}\,(v_i\, c) =$$

$$\frac{\partial}{\partial t}\left\{\phi S_w\left(1 + \frac{\rho_s(1-\phi)k_d}{\phi S_w}\, c\right\}\right. + \lambda\phi S_w\left\{1 + \frac{\rho_s(1-\phi)k_d}{\phi S_w}\right\}c - q\, c^* \qquad (24)$$

where k_d is the equilibrium constant.

Equation 24 can be written:

$$\frac{\partial}{\partial x_i}\left(D_{ij}\,\frac{\partial c}{\partial x_j}\right) - \frac{\partial}{\partial x_i}(v_i c) = \frac{\partial}{\partial t}(\phi S_w R c) + \lambda\phi S_w R c - q\, c^* \qquad (25)$$

where R is the retention factor defined as:

$$R = 1 + \frac{\rho_s(1-\phi)k_d}{\phi S_w} = 1 + \frac{\rho_b k_d}{\phi S_w} \qquad (26)$$

and ρ_b is the bulk density, $(1-\phi)\rho_s$.

Expanding equation 25, and using equation 26, assuming $\frac{\partial}{\partial t}(\rho_b k_d) = 0$:

$$\frac{\partial}{\partial x_i}(D_{ij}\frac{\partial c}{\partial x_j} - v_i\frac{\partial c}{\partial x_i} = \phi S_w R\,(\frac{\partial c}{\partial t} + \lambda c) + q(c - c^*) \qquad (27)$$

SATURN approximates equation 27 using the upstream weighted residual finite-element technique of Huyakorn and Nilkuha [1979]. The initial and boundary conditions of equation 27 can be written:

$$c(x_1,x_2,0) = c_0 \qquad (28)$$

$$c(x_1,x_2,t) = \hat{c} \text{ on } B_1' \qquad (29)$$

$$D_{ij}\frac{\partial c}{\partial x_j} n_i = q_c^D \text{ on } B_2' \qquad (30)$$

$$D_{ij}\frac{\partial c}{\partial x_j} n_i - v_i n_i c = q_c^T \text{ on } B_3' \qquad (31)$$

where B_1' is the portion of the boundary where the concentration is prescribed as $\hat{c}$, and B_2' and B_3' are portions of the boundary where the dispersive and total solute mass fluxes are prescribed as q_c^D and q_c^T, respectively.

GROUNDWATER FLOW SIMULATION

Prior to simulating infiltration from the canal, the applicability of the SATURN code to the hydrologic conditions at the RNM site (i.e. line infiltration through 200m of unsaturated alluvium) was assessed with test simulations. In the first simulation attempts, the medium was considered dry and the nodes representing the line source were assigned a specified flux equal to the observed canal transmission loss. When the solution failed to converge, the time step size was reduced. When further reduction in time step size was no longer practical, the moisture content of the medium was raised. All combinations of time step size and moisture content resulted in non-convergence when the line source was represented by specified flux nodes.

The line source nodes were then assigned a slight positive hydraulic head (+20 cm) and the medium was again assumed dry. As before, the solution did not converge. It appeared that the sharp saturated/unsaturated interface was the source of the numerical problem. The moisture content was raised to 20% (approximately 2/3 saturated) and convergence was rapid.

As a result of these test runs, the simulation strategy for the RNM canal was to represent the canal by constant head nodes. The initial moisture content of the alluvium was 20% and allowed to drain to approximately a steady state condition.

The RNM canal transmission loss is approximately .2 cm^3/sec/cm. Cambric tritium did not arrive at RNM-2S for approximately 1050 days after pumping was initiated. If the soil beneath the canal had a uniform porosity of .3 and was initially dry, it would only take about 380 days to completely saturate a column soil 10 m, wide from the canal to the water table at the observed canal infiltration rate. For this

reason, it is assumed that the flow system had reached steady-state prior to the arrival of Cambric tritium at RNM-2S.

Three indicators were used to determine when steady-state in the model was reached:

- No change in the moisture contents with time
- No change in the velocity field with time
- No change is storage (a net boundary flux close to 0)

At steady-state, and for all but the first few days of simulation, the flow at the constant head nodes representing the canal totaled 1.0×10^4 cm^3/day/cm. Because only one side of the canal was represented by the solution domain, the flow for each cm. of canal is then 2.0×10^4 cm^3/day/cm. The distance between flumes 1 and 3 is 1100 m. If the transmission losses were uniform between the flumes, the total loss for this section of canal would be 2×10^9 cm^3/day (2.3×10^4 cm^3/sec). Although slightly higher than the mean loss, this value lies within the observed values of the canal transmission losses as measured by the flume data (Figure 4).

At the beginning of the flow simulation, the solution domain was assumed to consist of a single, isotropic material with the hydraulic properties given earlier in this report. This assumption proved unsatisfactory as water rapidly accumulated in the system and a large groundwater mound soon developed beneath the canal. The net boundary flux was consistently positive indicating a net increase in storage. As the saturated--unsaturated interface rose into the larger elements, the solution became unstable and more iterations were required for convergence at each time step (Figure

20).

By increasing the horizontal hydraulic conductivity of the bottom three rows of nodes from 6.29×10^{-4} cm/sec to 6.29×10^{-3} cm/sec, ($k_{xx}/k_{zz} = 10$) the net boundary flux became negative, and the groundwater mound beneath the canal began to lower. As the saturated--unsaturated interface dropped, the solution instability rapidly decreased as seen in Figure 21.

Once the groundwater mound had been reduced to near the initial water level, the horizontal hydraulic conductivity in the bottom three rows of nodes was adjusted to bring the net boundary flux to near 0. This occurred when $k_{xx}/k_{zz} = 4.79$. When the net boundary flux was within 0.1%, the flow simulation was terminated. The steady-state moisture contents and velocity field were then used as input to the transport simulation. Figures 22 and 23 show the steady-state saturation values and velocity field, respectively.

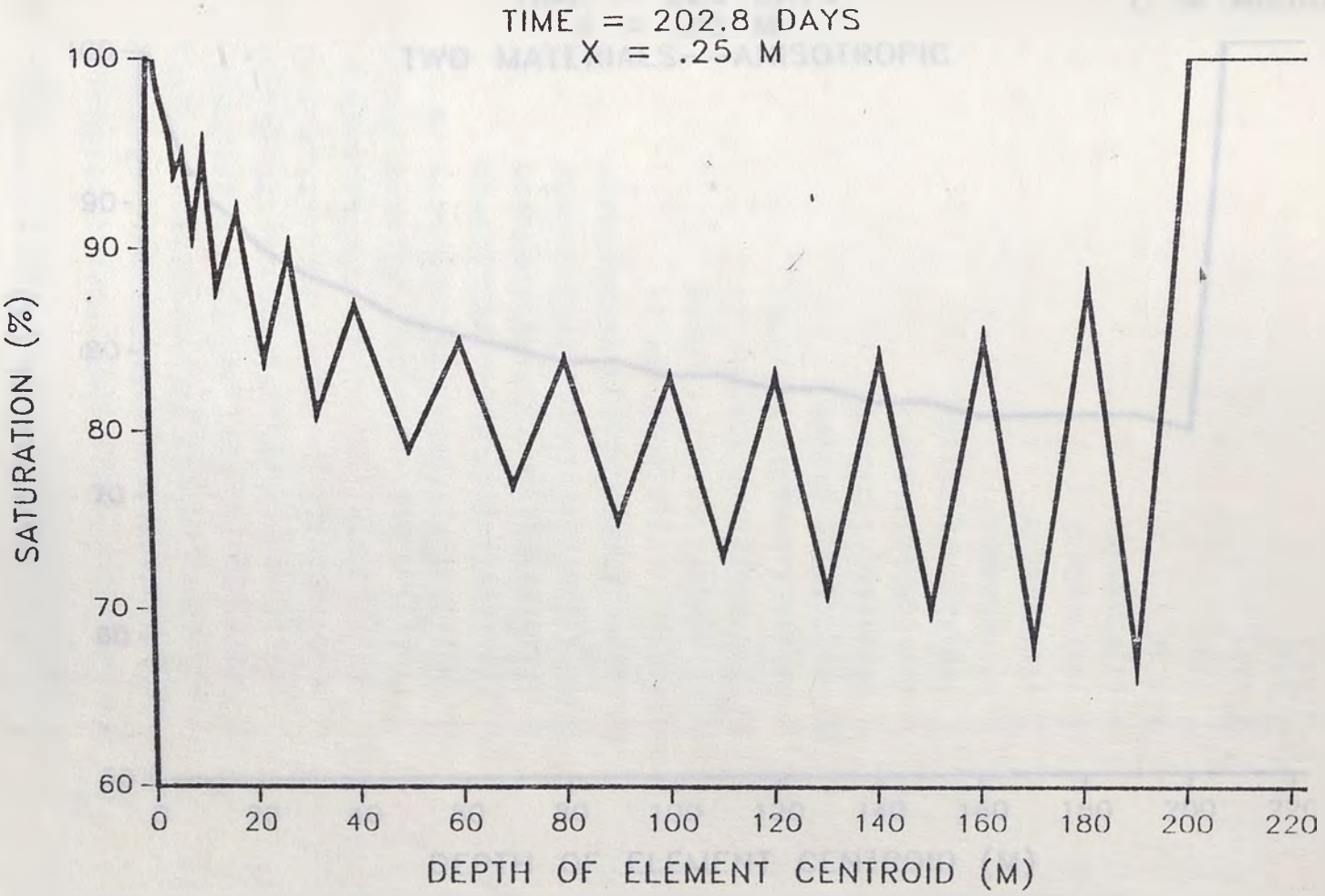

Figure 20. Graphical representation of numerical instabilities.

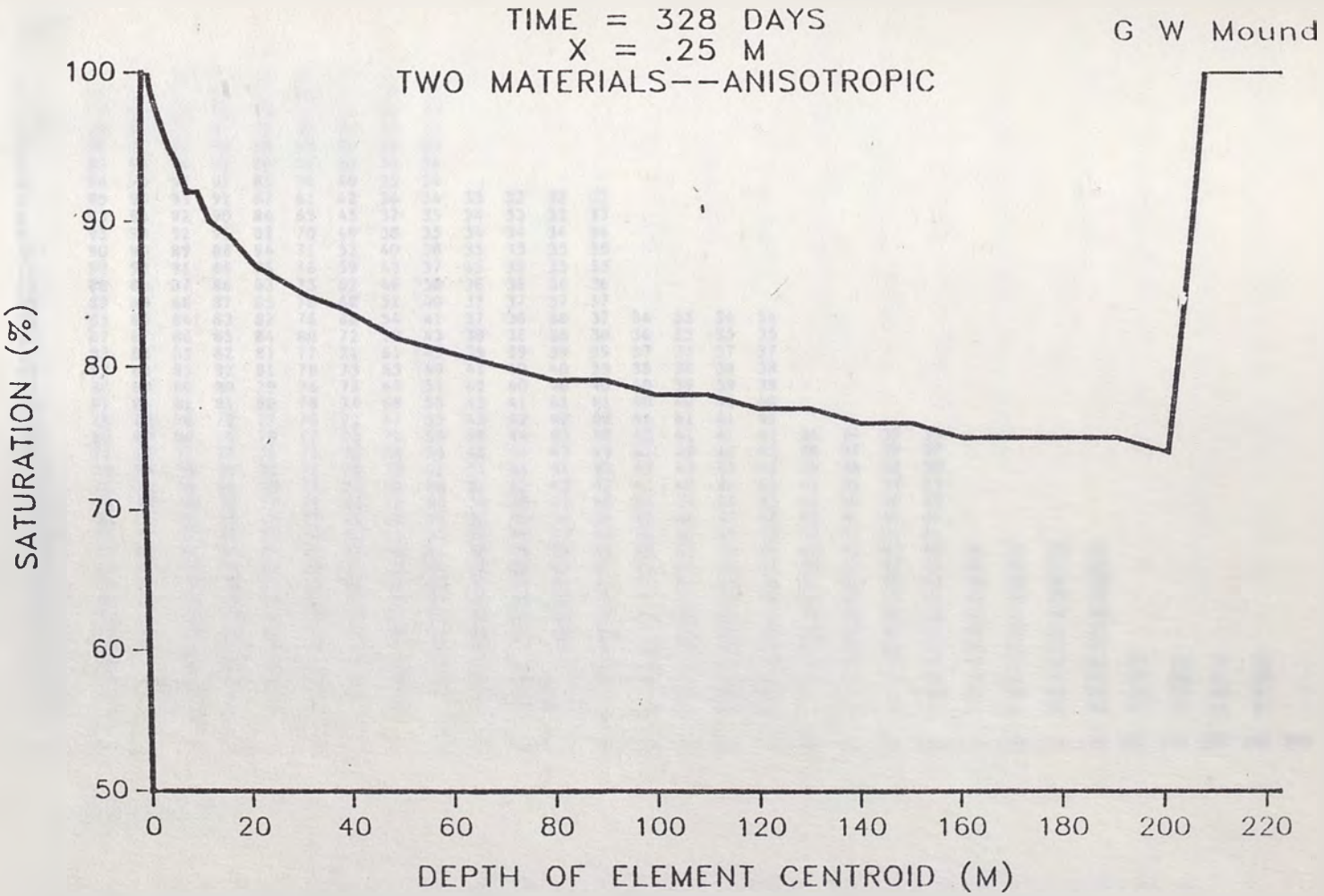

Figure 21. Effect of anisotropy on solution stability.

DEPTH (m)																															
0	**	**	98	77	54	38	33	32	32																						
0.5	**	**	97	88	63	40	34	33	32																						
1.0	**	99	97	90	70	42	35	33	33																						
1.5	99	98	96	91	75	45	35	33	33																						
2	98	97	95	91	80	48	36	34	33																						
3	97	96	94	91	84	52	38	34	34																						
4	96	95	93	91	85	56	40	35	34																						
5	95	95	93	91	87	61	42	36	34	33	32	32	32																		
6	93	93	92	90	86	65	45	37	35	34	33	33	33																		
8	93	93	92	91	87	70	49	38	35	34	34	34	34																		
10	90	90	89	88	84	71	52	40	36	35	35	35	35																		
12	92	92	91	89	86	76	59	43	37	35	35	35	35																		
15	88	88	87	86	83	75	62	46	38	36	36	36	36																		
20	89	88	88	87	85	78	68	51	40	37	37	37	37																		
25	85	85	84	83	82	76	68	54	41	37	38	38	37	34	33	34	34														
30	87	87	86	85	84	80	72	59	43	38	38	38	38	36	35	35	35														
35	83	83	82	82	81	77	71	61	45	39	39	39	39	37	37	37	37														
45	83	83	83	82	81	78	73	65	49	41	40	40	39	38	38	38	38														
55	80	80	80	80	79	76	72	65	51	42	40	40	40	40	39	39	39														
65	81	81	81	81	80	78	74	68	55	45	41	41	41	40	40	40	40														
75	78	78	78	78	77	76	72	67	55	45	42	42	42	41	41	41	41														
85	80	80	80	79	79	77	75	70	59	48	44	43	42	42	41	41	41	36	34	35	35										
95	77	77	77	77	76	75	72	68	58	48	44	43	43	42	42	42	42	38	37	37	37										
105	79	79	79	79	78	77	75	70	61	51	46	44	43	43	43	43	42	39	38	38	38										
115	76	76	76	76	75	74	72	68	60	51	45	43	43	43	43	44	43	41	39	39	39										
125	78	78	78	78	77	76	74	71	63	54	48	45	45	44	44	44	43	41	40	40	40										
135	75	75	75	75	74	73	71	68	61	52	46	44	44	44	44	44	43	42	41	41	41										
145	77	77	77	77	77	76	74	71	65	56	49	47	46	46	45	44	43	42	41	41	41										
155	74	74	74	74	74	73	71	68	61	54	48	45	44	44	44	44	44	43	43	43	42	36	34	35	35						
165	77	77	77	76	76	76	74	72	66	58	51	48	47	46	46	46	45	43	42	42	41	38	37	37	37						
175	74	74	74	73	73	72	71	68	62	55	49	46	45	44	44	44	44	44	44	44	43	40	38	38	38						
185	76	76	76	76	76	75	74	72	67	60	54	50	48	47	47	47	46	45	43	42	41	39	38	39	39						
195	73	73	73	73	72	72	70	67	62	56	50	46	45	45	45	45	45	44	44	45	45	42	41	40	40						
205	**	**	**	**	**	**	**	**	**	85	67	58	54	51	50	48	46	45	44	43	41	40	39	39	39						
210	**	**	**	**	**	**	**	**	**	**	**	**	**	**	**	**	**	**	92	62	50	46	43	42	41						
215	**	**	**	**	**	**	**	**	**	**	**	**	**	**	**	**	**	**	**	**	**	**	**	**	66	45	38	36	34		
217	**	**	**	**	**	**	**	**	**	**	**	**	**	**	**	**	**	**	**	**	**	**	**	**	**	98	61	44			
219	**	**	**	**	**	**	**	**	**	**	**	**	**	**	**	**	**	**	**	**	**	**	**	**	**	**	**	99			
220	**	**	**	**	**	**	**	**	**	**	**	**	**	**	**	**	**	**	**	**	**	**	**	**	**	**	**	**			
x(m)	0	.5	1	1.5	2	3	5	7	10	15	20	25	30	40	50	60	70	80	90	100	110	120	130	140	150	160	170	180	190	200	

* = greater than 99%

Figure 22. Simulated steady-state element saturation values (%).

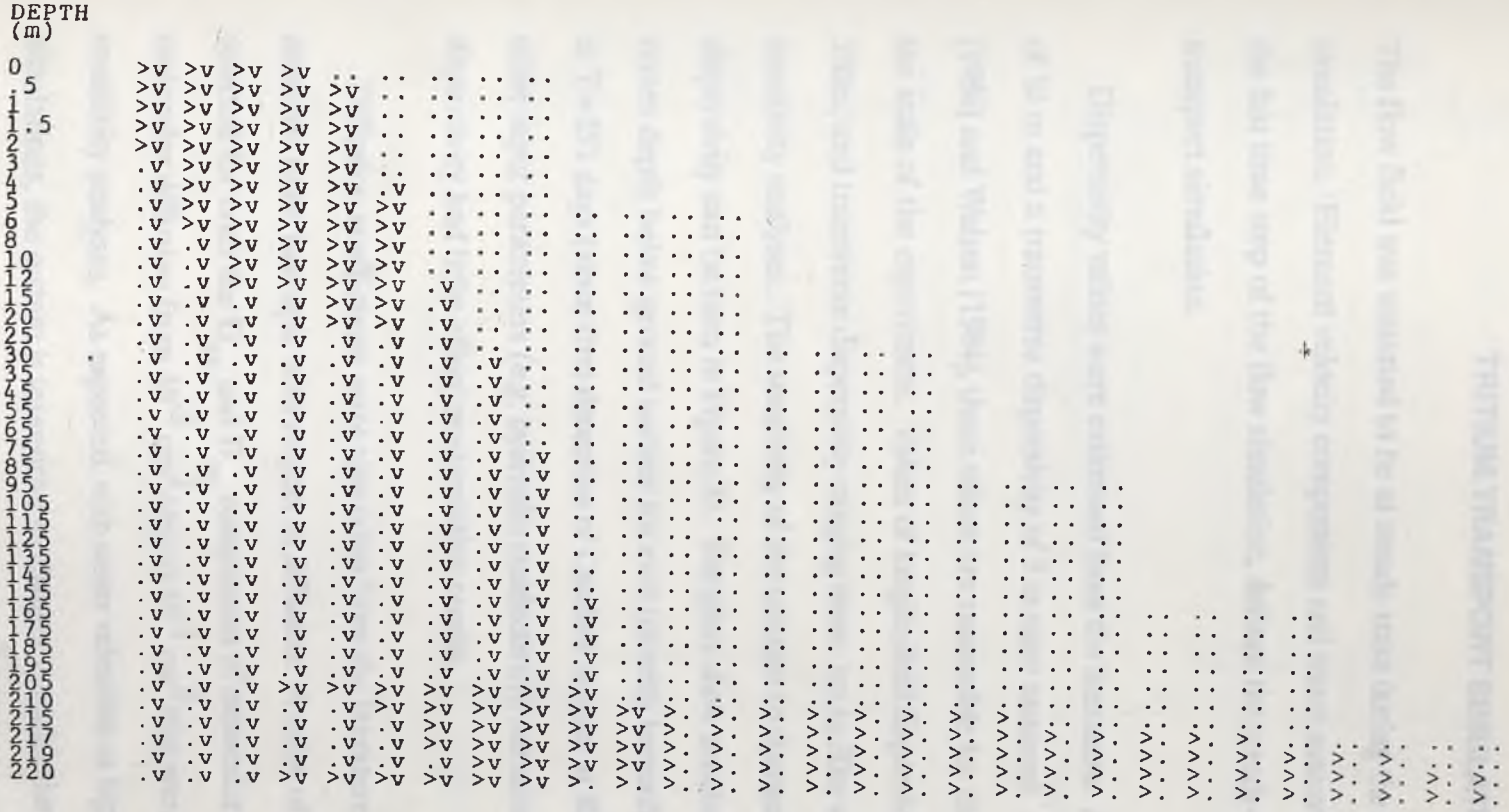

Figure 23. Qualitative representation of the vertical and horizontal components of the simulated steady-state flow field. Dots represent velocity components less than 1 cm/day.

TRITIUM TRANSPORT SIMULATION

The flow field was assumed to be at steady-state during the transport portion of the simulation. Element velocity components and water saturation data, determined in the last time step of the flow simulation, defined the steady-state condition for the transport simulation.

Dispersivity values were estimated from the literature. A longitudinal dispersivity of 10 m and a transverse dispersivity of 3 m were assumed. According to Gelhar [1986] and Walton [1984], these values are reasonable for the simulated medium and the scale of the experiment. Values of longitudinal dispersivity ranging from 1m to 100m, and transverse dispersivity ranging from .1m to 30m were simulated in sensitivity analyses. The sensitivity of the solution to changes in longitudinal dispersivity can be seen in Figure 24. The plots show simulated tritium concentration verses depth below ground surface for x=0 (directly beneath the center of the canal) at T=251 days (since first detection of Cambric tritium at RNM-2S). Relative to other input parameters (e.g. hydraulic conductivity), variations in longitudinal dispersivity had little effect on simulation results.

Diffusion coefficients were also taken from the literature. The medium was assumed to be isotropic with respect to diffusion. A value of 1.0×10^{-3} cm^2/day was selected for both the D_{xx} and D_{zz} components of molecular diffusion. Values of molecular diffusion from 10^{-5} cm^2/day to 10^{-1} cm^2/day were simulated in the sensitivity analyses. As expected, with water velocities as high as those in the simulations, the system is insensitive to changes in molecular diffusion coefficients.

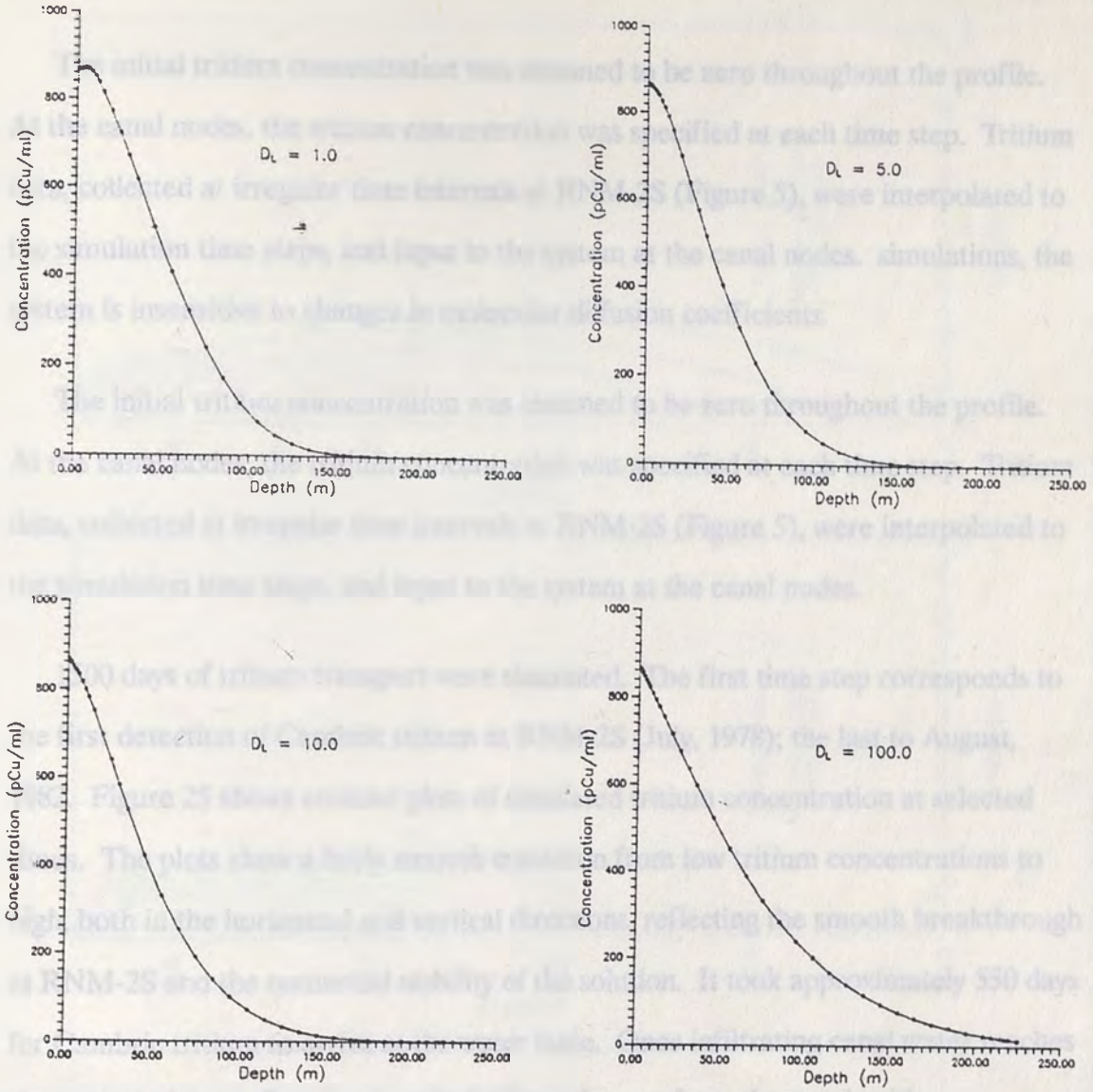

Figure 24. Solution sensitivity to changes in longitudinal dispersivity.

The initial tritium concentration was assumed to be zero throughout the profile. At the canal nodes, the tritium concentration was specified at each time step. Tritium data, collected at irregular time intervals at RNM-2S (Figure 5), were interpolated to the simulation time steps, and input to the system at the canal nodes. simulations, the system is insensitive to changes in molecular diffusion coefficients.

The initial tritium concentration was assumed to be zero throughout the profile. At the canal nodes, the tritium concentration was specified at each time step. Tritium data, collected at irregular time intervals at RNM-2S (Figure 5), were interpolated to the simulation time steps, and input to the system at the canal nodes.

1500 days of tritium transport were simulated. The first time step corresponds to the first detection of Cambric tritium at RNM-2S (July, 1978); the last to August, 1982. Figure 25 shows contour plots of simulated tritium concentration at selected times. The plots show a fairly smooth transition from low tritium concentrations to high, both in the horizontal and vertical directions, reflecting the smooth breakthrough at RNM-2S and the numerical stability of the solution. It took approximately 550 days for Cambric tritium to arrive at the water table. Once infiltrating canal water reaches the saturated zone, flow is primarily horizontal, away from the canal, with concentrations increasing with depth at about the same gradient as the horizontal concentration gradient in the unsaturated zone.

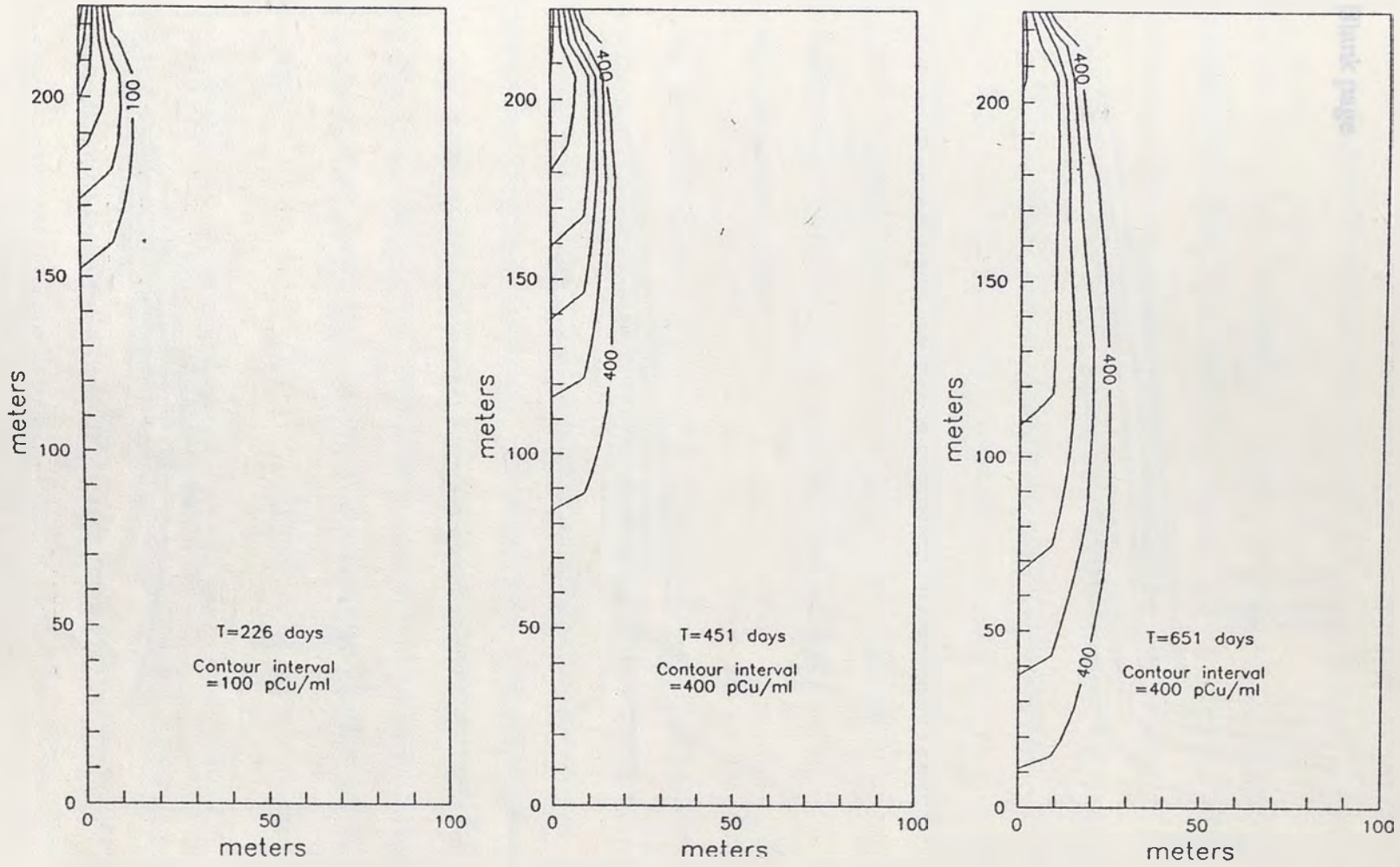

Figure 25. Contour plots of simulated tritium concentration at selected time steps.

Blank page

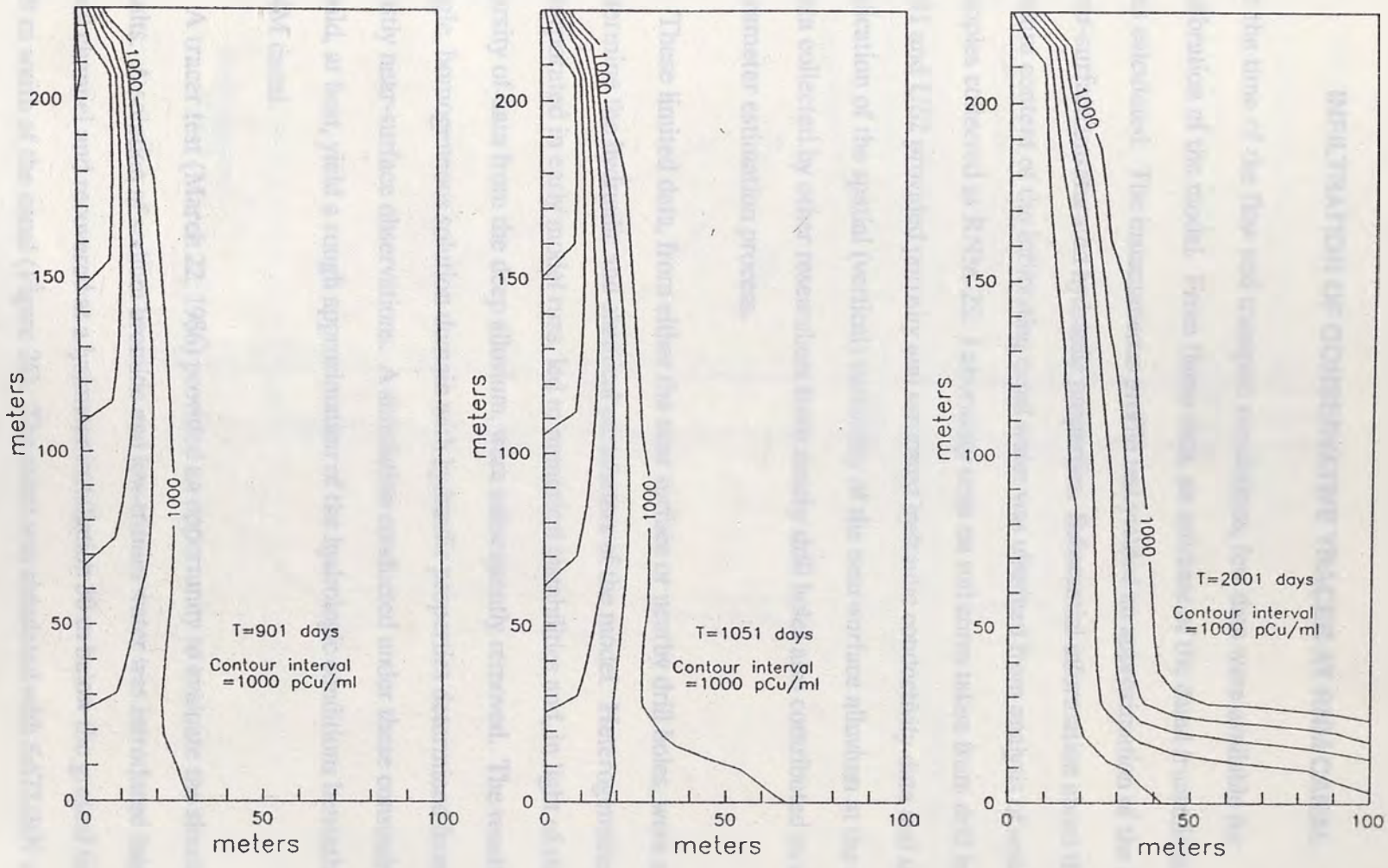

Figure 25 (cont.). Contour plots of simulated tritium concentration at selected time steps.

INFILTRATION OF CONSERVATIVE TRACER AT RNM CANAL

At the time of the flow and transport simulations, few data were available for calibration of the model. From flume data, an estimate of the canal transmission loss was calculated. The instantaneous profile test yielded an approximation of the bulk, near-surface unsaturated hydraulic properties. Substantial information about the tritium content of the infiltrating canal water was obtained from analysis of water samples collected at RNM-2S. Laboratory tests on soil cores taken from drill holes US1 and US2 provided porosity and saturated hydraulic conductivity data and some indication of the spatial (vertical) variability of the near-surface alluvium at the canal. Data collected by other researchers from nearby drill holes also contributed to the parameter estimation process.

These limited data, from either the near surface or nearby drill holes, were used to determine the hydraulic and chemical parameters of the model. Heterogeneities, incorporated in early model runs, led to numerical instabilities and, in light of the sparsity of data from the deep alluvium, were subsequently removed. The result was a single, homogeneous solution domain with hydraulic properties determined from mostly near-surface observations. A simulation conducted under these constraints would, at best, yield a rough approximation of the hydrologic conditions beneath the RNM canal.

A tracer test (March 22, 1986) provided an opportunity to evaluate the simulation results. A solution of sodium bromide and low-tritium water was introduced into the canal channel and recovered at a lysimeter installation 30 m below the ground surface, 28.9 m south of the canal (Figure 26). The event was simulated with SATURN using

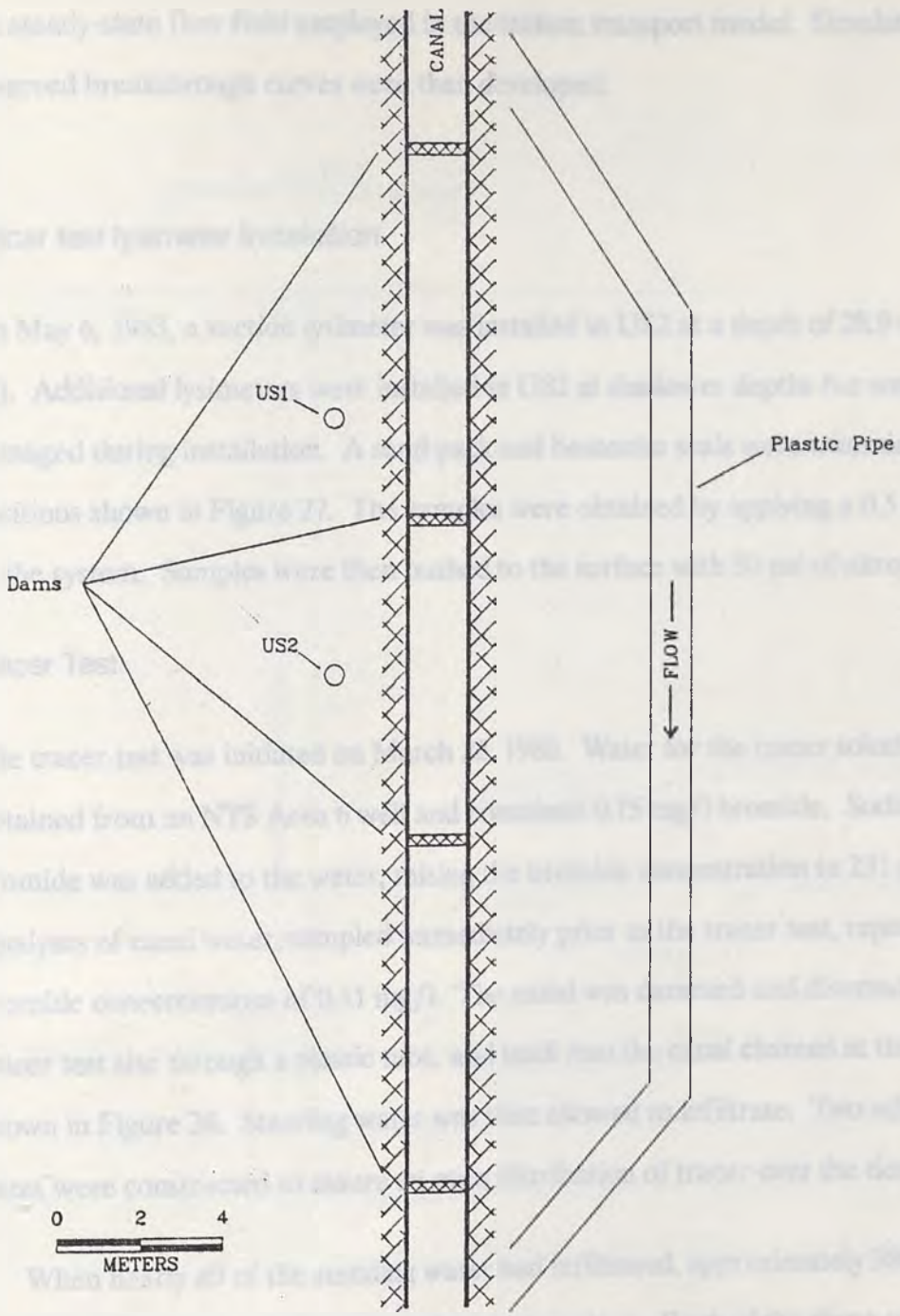

Figure 26. Tracer Test Site.

the steady-state flow field employed in the tritium transport model. Simulated and observed breakthrough curves were then developed.

Tracer test lysimeter Installation

On May 6, 1985, a suction lysimeter was installed in US2 at a depth of 28.9 m (Figure 26). Additional lysimeters were installed in US2 at shallower depths but were damaged during installation. A sand pack and bentonite seals were trimmied into the positions shown in Figure 27. The samples were obtained by applying a 0.5 bar suction to the system. Samples were then pushed to the surface with 50 psi of nitrogen.

Tracer Test

The tracer test was initiated on March 22, 1986. Water for the tracer solution was obtained from an NTS Area 6 well and contained 0.15 mg/l bromide. Sodium bromide was added to the water, raising the bromide concentration to 231 mg/l. Analyses of canal water, sampled immediately prior to the tracer test, reported a bromide concentrations of 0.11 mg/l. The canal was dammed and diverted around the tracer test site through a plastic tube, and back into the canal channel at the location shown in Figure 26. Standing water was then allowed to infiltrate. Two additional dams were constructed to assure an even distribution of tracer over the desired length

When nearly all of the standing water had infiltrated, approximately 3800 l of tracer solution was introduced into the canal sections. Each of the three sections received about one third of tracer solution. After 5.5 hours, the tracer solution had infiltrated, and the canal was undamed and flow was returned to the channel.

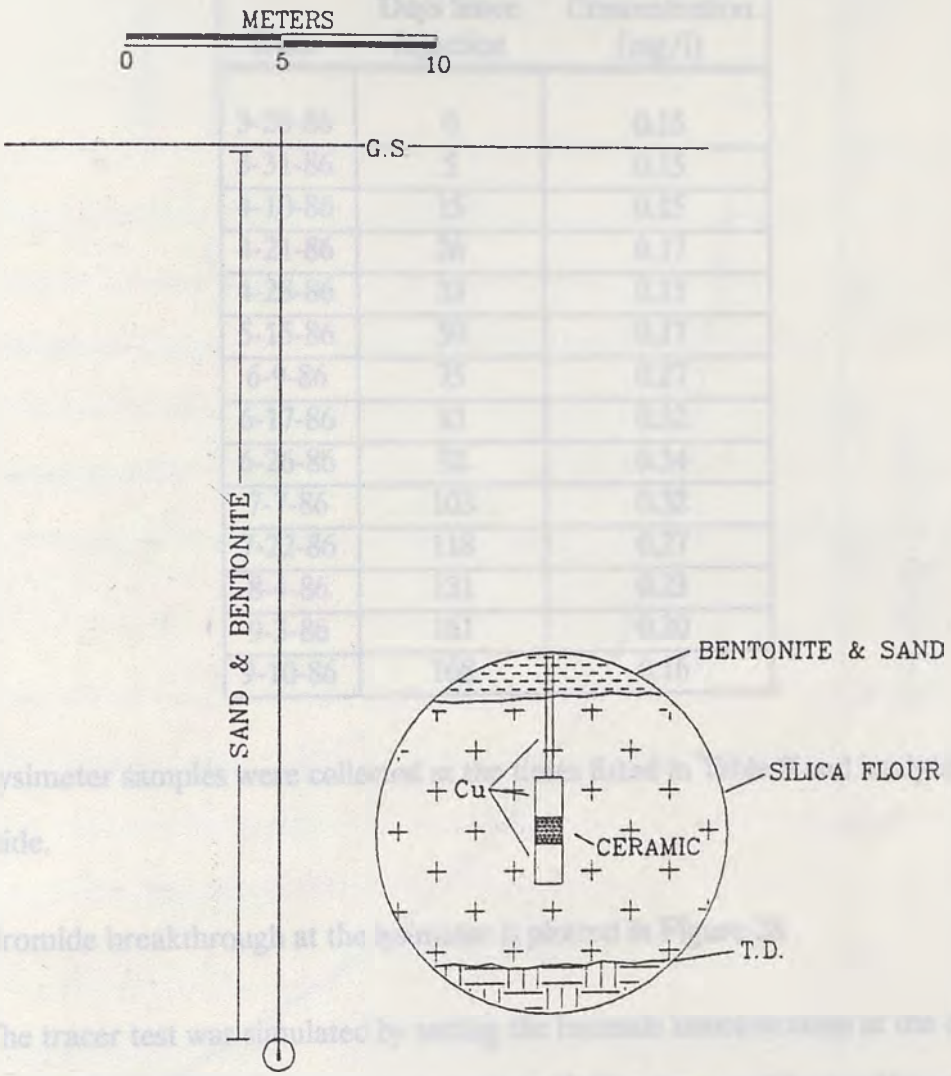

Figure 27. Suction Lysimeter installation.

TABLE 8. Results of Lysimeter Sampling

Date	Days Since Injection	Bromide Concentration (mg/l)
3-26-86	0	0.15
3-31-86	5	0.15
4-10-86	15	0.15
4-21-86	26	0.17
4-28-86	33	0.15
5-15-86	50	0.17
6-9-86	75	0.27
6-17-86	83	0.32
6-26-86	92	0.34
7-7-86	103	0.32
7-22-86	118	0.27
8-4-86	131	0.23
9-3-86	161	0.20
9-10-86	168	0.16

Lysimeter samples were collected at the times listed in Table 8 and analyzed for bromide.

Bromide breakthrough at the lysimeter is plotted in Figure 28.

The tracer test was simulated by setting the bromide concentration at the canal nodes to 230 mg/l for the appropriate number of time steps, and by specifying node 583, which is in the same location (in the finite element grid) as the lysimeter, as an observation node.

Although the simulated breakthrough curve has the same basic shape and maximum concentration as the observed data, the model predicted a much earlier

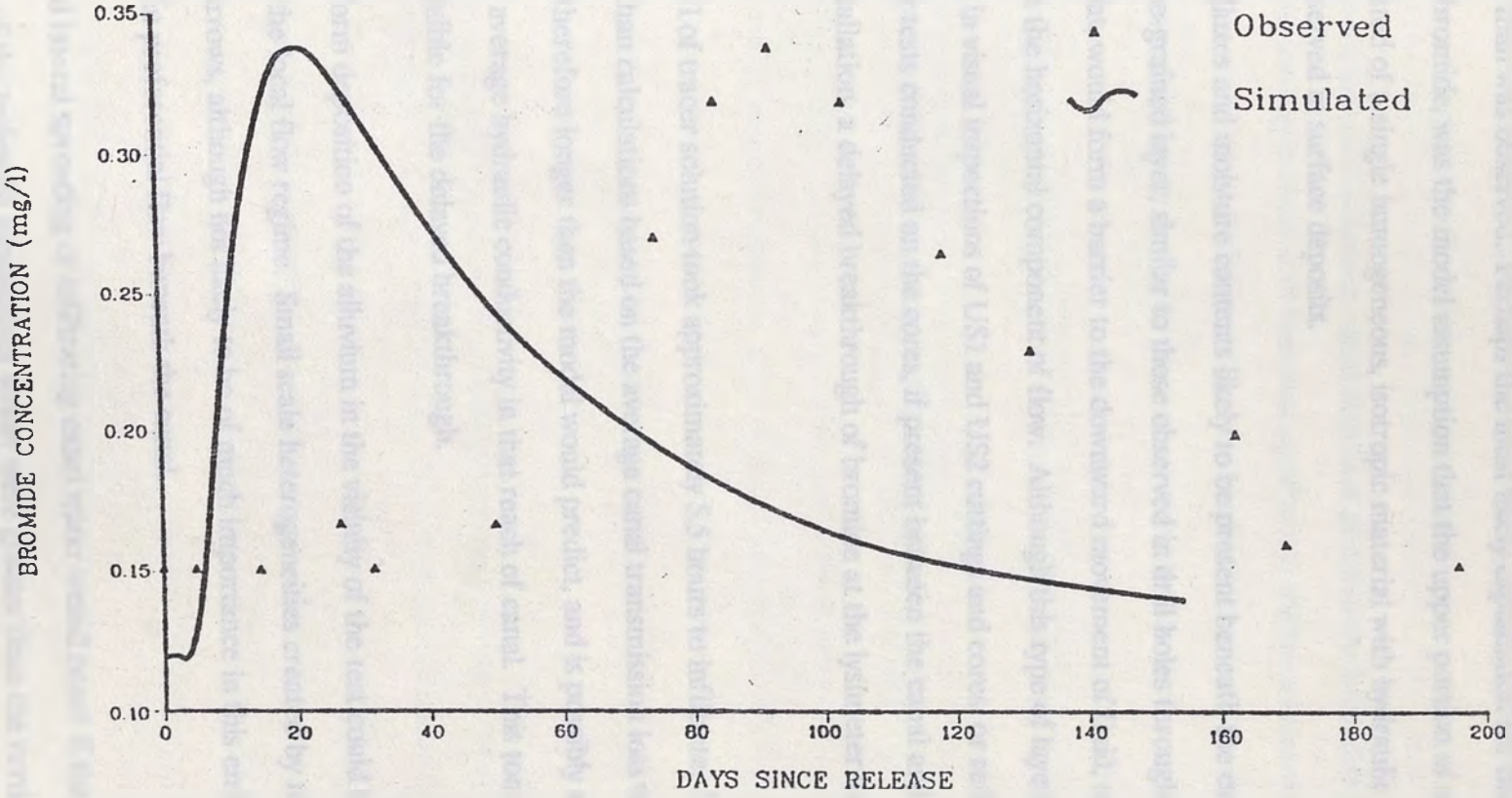

Figure 28 Plot showing simulated and observed bromide concentration.

breakthrough than was observed. Perhaps the most likely explanation for the delayed arrival of the bromide, was the model assumption that the upper portion of solution domain consisted of a single homogeneous, isotropic material with hydraulic properties observed in surface deposits.

With the fluxes and moisture contents likely to be present beneath the canal, a horizontal fine-grained layer, similar to those observed in drill holes throughout Frenchman flat, would form a barrier to the downward movement of fluid, resulting in an increase in the horizontal component of flow. Although this type of layering was not observed in visual inspections of US1 and US2 cuttings and cores, or reflected in permeameter tests conducted on the cores, if present between the canal and the lysimeter installation, a delayed breakthrough of bromide at the lysimeter would occur.

The 3800 l of tracer solution took approximately 5.5 hours to infiltrate. This is 25% longer than calculations based on the average canal transmission loss would predict, and therefore longer than the model would predict, and is possibly a result of a lower than average hydraulic conductivity in that reach of canal. This too may be partly responsible for the delayed breakthrough.

Non-uniform deposition of the alluvium in the vicinity of the test could be expected to influence the local flow regime. Small scale heterogeneities created by root cavities or animal burrows, although not likely to be of much importance in this environment, could result in preferential flow beneath the canal.

Increased lateral spreading of infiltrating canal water would occur if the horizontal components of the hydraulic conductivity tenser were greater than the vertical

component. Such anisotropy, although common in alluvial environments, was not incorporated into the upper portion of the solution domain.

An improperly installed lysimeter could also have affected the breakthrough. If the diameter or the depth of the drill hole was significantly different from the values used to calculate the sand pack and grout locations and volumes, or if bends in the lysimeter tubes resulted in an improper placement of the lysimeter, the porous cup might not be in contact with the sand pack and might even be grouted-off from the formation. Bridging in the drill hole could also result in an improper placement of the grout and sand pack. Although it is unlikely that faulty lysimeter installation is entirely responsible for the delayed breakthrough, it could have been a factor.

CONCLUSIONS

According to the simulation results it would take approximately 550 days for Cambric tritium to travel from the canal to the water table. The perforations of RNM-2S are at approximately 100m below the static water level (230 m below ground surface). Assuming a porosity of .3, the volume of water in a saturated sphere of radius 100m would be

$$(.3)\,\frac{4}{3}\,\pi\,(100\text{m})^3 = 1.26 \times 10^6\ \text{m}^3 \qquad (32)$$

At the pumping rates of RNM-2S ($2\text{m}^3/\text{min}$), $1.82 \times 10^6\text{m}^3$ would be pumped in 550 days. Cambric tritium was first detected at RNM-2S after $2.3 \times 10^6\text{m}^3$ had been pumped. If the simulation results were accurate, and if the saturated zone in the vicinity of RNM-2S was homogeneous and isotropic with a porosity of .3, then the first arrival of recirculated tritium at RNM-2S would occur after approximately $5 \times 10^6\text{m}^3$ had been pumped. As can been seen in Figure 7, this is coincident with the peak in observed tritium concentration at RNM-2S.

This estimate assumes transport in a homogeneous and isotropic medium. Any departure from this assumption would increase the arrival time of recirculated tritium at RNM-2S. Results of the tracer test and observations made throughout Frenchman Flat (and alluvial basins in general) support the existence of heterogeneities in the flow system. In light of the above calculations, it appears unlikely that Cambric tritium, infiltrating from the RNM canal and recaptured by RNM-2S, had a significant effect on the breakthrough of tritium at RNM-2S.

Beyond providing a basis for evaluating the potential impact of infiltrating canal water on tritium breakthrough at RNM-2S, these simulations will hopefully contribute to the general understanding of flow and transport processes at the RNM site. If the model assumptions were valid (the canal is underlain by a single homogeneous, isotropic medium with the hydraulic characteristics selected for the model; the stated initial and boundary conditions accurately describe the physical system; flow is steady-state; the governing equations of flow and solute transport used in the numerical model are valid), the model would correctly simulate the movement of water and tritium beneath the RNM canal.

Understanding that the above assumptions are not entirely valid, the simulations provide a point of reference from which estimates of the behavior of water and solutes in more realistic (and hence more complicated) systems can be made.

LITERATURE CITED

Black, T.A., W.R. Gardner, and G.W. Thurtell. 1969. The prediction of evaporation, drainage and soil water storage for a bare soil. *Soil Sci. Soc. Amer. Proc.* **33**, pp. 655-660.

Brooks, R.H., and A.T. Corey. 1964. "Hydraulic properties of porous media". Hydrol. Pap. 3, Colo. State Univ., Fort Collins.

Bruce, R.R., and A. Klute. 1956. The measurement of soil moisture diffusivity. *Soil Sci. Soc. Amer. Proc.* **20**, pp. 458-462.

Brutsaert, W. 1967. Some Methods of calculating unsaturated permeability. *Trans. ASAE* **10**, pp. 400-404.

Cassel, D.K., A.W. Warrick, D.R. Nielson, and J.W. Biggar. 1968. Soil water diffusivity values based upon time dependent soil water content distributions. *Soil Sci. Soc. Amer. Proc.* **32**, pp. 774-777.

Childs, E.C., and N. Collis-George. 1950. The permeability of porous materials. *Proc. Roy. Soc., Ser. A* **201**, pp. 392-405.

Davidson, J.M., L.R. Stone, D.R. Nielson, and M.E. Larue. 1969. Field measurement and use of soil properties. *Water Resources Res.* **5**, pp. 1312-1321.

Doering, E.J. 1965. Soil Water Diffusivity by the one-step method. *J. Soil Sci.* **99**, pp. 322-326.

Farrell, D.A., and W.E. Larson. 1972. Modeling the pore structure of porous media. *Water Resources Res.* **8**, pp. 699-706.

Fenneman, N.M. 1931. "Physiography of Western United States". Mcgraw-Hill, New York.

Flocher, W.J., M. Yamaguchi, and D.R. Nielson. 1968. Capillary conductivity and soil water diffusivity values from vertical soil columns. *Agron. J.* **60**, pp. 605-610.

Gardner, W.R. 1956. Calculation of capillary conductivity from pressure plate outflow data. *Soil Sci. Soc. Amer. Proc.* **20**, pp. 317-320.

Gardner, W.R. 1970. Field measurement of soil water diffusivity. *Soil Sci. Soc. Amer. Proc.* **20**, pp. 832-833.

Gelhar, L.W. 1986. Stochastic subsurface hydrology from theory to applications. *Water Resources Res.* **22**, pp. 135S-145S.

Hillel, D. 1971. "Soil and water: physical principles and processes". Academic Press, Inc., New York.

Hillel, D., V.D. Krentos, Y. Stylianou. 1972. Procedure and test of an internal drainage method for measuring soil hydraulic characteristics in situ. *J. Soil Science* **114**, pp. 395-400.

Hoffman, D. C., R. Stone, W.W. Dudley. 1977. Radioactivity in the underground environment of the Cambric nuclear explosion at the Nevada Test Site. Rep. LA-6877-MS. Los Alamos Scientific Lab. Los Alamos, New Mexico

Huyakorn, P.S. and K. Nilkuha. 1979. Solution of transient transport equation using an upstream finite element scheme. *Appl. Math. Modeling* **3**, pp. 7-17.

Huyakorn, P.S., S.D. Thomas, J.W. Mercer, B.H. Lester. 1983. "SATURN: A finite element model for simulating saturated-unsaturated flow and radionuclide transport". Technical Report by GeoTrans Inc., Reston, Virginia.

Jackson, R.D., R.F. Reginato, and C.H.M. Van Bavel. 1963. Examination of the pressure plate outflow method for measuring capillary conductivity. *J. Soil Sci.* **96**, pp. 249-256.

Jackson, R.D., R.F. Reginato, and C.H.M. Van Bavel. 1965. Comparison of measured and calculated hydraulic conductivities of unsaturated soils. *Water Resources Res.* **1**, pp. 375-380.

Jones, A.J., and R.J. Wagenet. 1984. In situ estimation of hydraulic conductivity using simplified methods. *Water Resources Res.* **20**, pp. 1620-1626

Klute, A. 1972. The determination of the hydraulic conductivity and diffusivity of unsaturated soils. *J. Soil Sci.* **113**, pp. 264-276.

Kunze, R.J., and D. Kirkham. 1962. Simplified accounting for membrane impedance in capillary conductivity determinations. *Soil Sci. Soc. Amer. Proc.* **26**, pp. 421-426.

Kunze, R.J., G. Uehara, and K. Graham. 1968. Factors important in the calculation of hydraulic conductivity. *Soil Sci. Soc. Amer. Proc.* **32**, pp. 760-765.

Marshall, T.J. 1958. A relation between permeability and size distribution of pores. *J. Soil Sci.* **9**, pp.1-8.

Mualem, Y. 1976. A new model for predicting the hydraulic conductivity of unsaturated porous media. *Water Resources Res.* **12**, June, pp. 513-522.

Miller, E.E., and D.E. Elrick. 1958. Dynamic determination of capillary conductivity extended for non-negligible membrane impedance. *Soil Sci. Soc. Amer. Proc.* **22**, pp. 483-486

Millington, R.J., and J.P. Quirk. 1961. Permeability of porous solids. *Trans. Faraday Soc.* **57**, pp. 1200-1206.

Nielson, D.R., J.M. Davidson, J.W. Biggar, and R.J. Miller. 1962. Water movement through Panoche clay loam soil. *Hilgardia* **35**, pp. 491-506.

Ogata, G., and L.A. Richards. 1957. Water content changes following irrigation of bare field soil that is protected from evaporation. *Soil Sci. Soc. Amer. Proc.* **21** , pp. 355-356.

Peek, A.J. 1966. Diffusivity determination by a new outflow method. in *Water in the unsaturated zone.* V ol. I, Publ. No. 82, Int. Assoc. Sci. Hydrol, pp.191-202

Richards, L.A., W.R. Gardner, and G. Ogata. 1956. Physical processes determining water loss from soil. *Soil Sci. Soc. Amer. Proc.* **20** , pp. 310-314.

Richards, S.J., and L.V. Weeks. 1953. Capillary conductivity values from moisture yield and tension measurements on soil collumns. *Soil Sci. Soc. Amer. Proc.* **17** , pp. 206-209.

Rijtema, P.E. 1959. Calculation of capillary conductivity from pressure plate outflow data with non-negligible membrane impedance. *Netherlands J. Agric. Sci.* **7** , pp. 209-215.

Rogers, J.S., and A. Klute. 1971. The hydraulic conductivity water content relationship during non-steady flow through a sand column. *Soil Sci. Soc. Amer. Proc.* **35** , pp. 695-700.

Romney, E.M., V.Q. Hale, A. Wallace, O.R. Hunt, J.D. G.V. Alexander, J.E. Kinnear, and T.L. Ackerman. 1973. "Some characteristics of soil and perennial vegetation in northern Mojave Desert areas of the Nevada Test Site". Rep. UCLA #12-916. UCLA, Los Angeles, Ca.

Rose, C.W., W.R. Stern, and J.E. Drummond. 1965. Determination of hydraulic conductivity as a function of depth and water content for soil in situ. *Aust. J. Soil Res.* **3** , pp. 1-9.

Sisson, J.B., A.H. Ferguson, and M. Th. van Genuchten. 1980. Simple Method for predicting drainage from field plots. *Soil Sci. Soc Amer. J.* **44** , pp. 1147-1152.

Vachaud, G. 1967. Determination of the hydraulic conductivity of unsaturated soils from an analysis of transient flow data. *Water Resources Res.* **3** , pp. 697-705.

Vachaud, G., and Jean-Louis Thony. 1971. Hysteresis during infiltration and redistribution in a soil column at different initial water contents. *Water Resources Res.* **7** , pp. 111-127.

van Bavel, C.H.M., G.B. Stirk, and K.J. Brust. 1968a. Hydraulic properties of a clay loam soil and the field measurement of water uptaken by roots. I Interpretation of water content and pressure profiles. *Soil Sci. Soc. Amer. Proc.* **32** , pp. 310-317.

van Bavel, C.H.M., K.J. Brust, and G.B. Stirk. 1968b. Hydraulic properties of a clay loam soil and the field measurement of water uptaken by roots. II The water balance of the root zone. *Soil Sci. Soc. Amer. Proc.* **32** , pp. 317-321.

van Genuchten, R. 1978. "Calculating the unsaturated hydraulic conductivity with a new, closed form analytical model". Dep. Civ. Eng., Princeton Univ., Princeton,

N.J., Water Resources Prog. Rep. 78-WR-08, 63 pp.

Walton, W.C. 1984. "Practical aspects of groundwater modeling". National Water Well Association.

Watson, K.K. 1966. An instantaneous profile method for determining the unsaturated hydraulic conductivity of porous materials. *Water Resources Res.* **2** , pp. 709-715.

Weeks, L.V., and S.J. Richards. 1967. Soil water properties computed from transient flow data. *Soil Sci. Soc. Amer. Proc.* **31** , pp. 721-725

Winograd, I.J., W. Thordarson, R.A. Young. 1971. "Hydrology of the Nevada Test Site and vicinity, Southeastern Nevada". U.S. Geol. Survey Open File Report.

Neutron Hole N1										
Time (hrs.)	Depth (cm)									
	45	75	105	135	165	195	225	255	300	320
0.	0.689	0.668	0.615	0.468	0.398	0.618	0.678	0.573	-	0.657
0.50	0.675	0.671	0.595	0.463	0.389	0.610	0.657	0.571	-	0.642
1.00	0.678	0.650	0.596	0.446	0.370	0.610	0.657	0.574	-	0.666
1.42	0.666	0.648	0.582	0.436	0.381	0.599	0.641	0.552	0.551	0.632
2.50	0.659	0.653	0.586	0.437	0.379	0.588	0.657	0.553	-	0.617
3.50	0.639	0.640	0.585	0.442	0.370	0.576	0.629	0.569	0.553	0.594
6.00	0.615	0.638	0.575	0.413	0.369	0.556	0.620	0.545	0.531	0.571
10.00	0.557	0.620	0.556	0.391	0.341	0.541	0.574	0.525	0.533	0.566
20.00	0.480	0.578	0.527	0.368	0.323	0.500	0.539	0.528	0.506	0.527
24.25	0.474	0.558	0.531	0.371	0.334	0.467	0.528	0.514	0.515	0.511
30.50	0.487	0.552	0.525	0.359	0.323	0.482	0.524	0.523	0.503	0.505
43.50	0.463	0.521	0.500	0.352	0.322	0.454	0.513	0.510	0.495	0.493
75.00	0.441	0.500	0.479	0.332	0.317	0.440	0.488	0.506	0.460	0.473
169.00	0.407	0.465	0.453	0.302	0.298	0.403	0.417	0.472	-	0.428
336.50	0.399	0.444	0.428	0.294	0.283	0.392	0.403	0.453	-	0.394
552.00	0.398	0.446	0.422	0.290	0.296	0.377	0.392	0.441	0.390	0.396

Neutron Hole N2										
Time (hrs.)	Depth (cm)									
	45	75	105	135	165	195	225	255	300	320
1.42	0.729	0.715	0.634	0.505	0.520	0.599	0.553	0.510	-	0.640
3.67	0.704	0.680	0.613	0.475	0.513	0.571	0.549	0.511	0.512	0.619
6.00	0.641	0.673	0.586	0.468	0.502	0.553	0.541	0.495	0.499	0.587
10.00	0.565	0.634	0.565	0.450	0.479	0.529	0.520	0.489	0.497	0.548
20.00	0.487	0.578	0.532	0.414	0.440	0.518	0.499	0.457	0.462	0.502
24.25	0.484	0.557	0.509	0.420	0.439	0.493	0.502	0.465	0.451	0.515
30.50	0.493	0.581	0.515	0.407	0.418	0.505	0.487	0.452	0.455	0.491
43.50	0.466	0.524	0.475	0.387	0.406	0.467	0.477	0.423	0.415	0.460
75.00	0.414	0.501	0.455	0.385	0.402	0.470	0.443	0.418	0.410	0.443
169.00	0.407	0.457	0.435	0.369	0.378	0.439	0.427	0.385	-	0.414
336.00	0.389	0.439	0.428	0.345	0.375	0.423	0.395	0.370	-	0.400
552.00	0.390	0.425	0.424	0.343	0.361	0.406	0.402	0.372	0.338	0.386

Time (hrs.)	Tensiometer Data (cm)									
	Array 1					Array 2				
	Tensiometer Depths (cm)									
	26	56	85	144	214	26	56	85	144	214
	Tensiometer Lengths (cm)									
	35	65	95	156	250	35	65	95	156	250
.25	5.50	5.50	8.50	15.50	24.00	4.50	6.00	12.00	17.00	24.00
.75	8.00	8.50	10.50	16.00	24.00	8.00	8.50	13.50	18.00	24.00
1.25	9.00	9.00	11.00	16.00	24.00	8.50	9.50	14.00	18.00	24.00
1.75	10.00	10.00	11.50	17.00	25.00	10.00	10.00	14.00	18.50	25.00
2.75	10.00	10.00	12.00	17.50	25.50	10.00	11.00	14.50	18.00	25.50
3.75	10.00	10.50	11.50	18.00	25.50	10.00	11.00	15.50	19.00	25.50
6.25	11.00	10.00	11.50	18.50	26.00	12.00	13.00	15.50	19.00	26.00
10.25	12.00	11.00	11.50	18.50	26.50	12.50	14.00	17.00	19.50	26.50
20.25	14.00	12.00	12.00	20.00	28.00	14.00	15.00	18.00	20.00	28.00
24.5	14.00	15.50	15.50	20.00	28.00	14.00	16.00	19.00	20.50	28.00
32.75	14.00	14.00	14.00	20.00	28.00	15.00	16.50	18.00	21.00	28.00
45.75	15.00	12.00	12.00	20.00	29.00	15.00	17.00	19.50	21.00	29.00
77.25	16.00	16.50	16.50	21.00	30.00	16.50	18.00	21.00	22.00	30.00
171.25	18.00	17.00	17.00	22.00	30.00	18.00	20.00	22.00	23.00	30.00
338.75	14.00	20.00	20.00	24.00	32.00	20.00	22.00	24.00	24.00	32.00
554.75	20.00	22.00	23.00	25.00	32.00	21.00	22.00	24.00	24.00	32.00

Flow rates (cc/sec)		
Inflow	Outflow tube 1	Outflow tube 2
943.4	368.8	150.2
857.9	372.7	150.1
877.0	370.5	149.0

Rate of Water Level Drop on Plot			
stage (cm)	time (min)	stage (cm)	time (min)
7.31	9	4.57	41
6.40	18	4.26	45
6.09	23	3.96	48
5.79	28	3.65	52
5.48	31	3.35	56
5.18	34	3.04	59
4.87	38	2.74	64